

ACCESSING CEREBRAL HEMODYNAMIC WITH MULTIMODAL IMAGING

by
Ho-Ching Yang

A Dissertation

Submitted to the Faculty of Purdue University

In Partial Fulfillment of the Requirements for the degree of

Doctor of Philosophy



Weldon School of Biomedical Engineering

West Lafayette, Indiana

May 2021

THE PURDUE UNIVERSITY GRADUATE SCHOOL
STATEMENT OF COMMITTEE APPROVAL

Dr. Yunjie Tong, Chair

Weldon School of Biomedical Engineering

Dr. Yu-Chein Wu

Indiana University School of Medicine

Dr. Joseph Rispoli

Weldon School of Biomedical Engineering

Dr. Joaquín Goñi Cortés

Weldon School of Biomedical Engineering and School of Industrial Engineering

Approved by:

Dr. George R. Wodicka

*In the hopes that this work may in some way contribute to future exploration of brain diseases,
which cannot be prevented or treated.*

ACKNOWLEDGMENTS

I would like to thank Purdue University, Weldon School of Biomedical Engineering, and my advisor, Dr. Yunjie Tong for offering me the unimaginable opportunity to complete my study here. I would like to thank Dr. Yu-Chein Wu for supporting, advising me, and allowing me to bridge my current knowledge to my future research. Also, I want to thank Dr. Joseph Rispoli for supporting and collaborating. I want to thank Dr. Joaquin Goni. I'm still using his independent component analysis, *connICA*, which is very useful. I would like to thank all my lab members and friends I met during these four years for all the useful suggestions and collaboration. I enjoyed the time having research with all of you. I want to express my gratitude to my family for encouraging and helping me. I really appreciate that my parents for allowing me studied abroad for years, although they missed me a lot.

TABLE OF CONTENTS

LIST OF FIGURES	8
ABSTRACT.....	12
1. BACKGROUND	13
2. STUDY 1	14
2.1 Introduction.....	14
2.2 Method	15
2.2.1 Data selection.....	15
2.2.2 Image acquisition.....	16
2.2.3 Data processing.....	16
2.2.4 Vascular measures	17
2.2.5 Cerebral circulation	17
2.2.6 Cerebral blood density (volume)	18
2.2.7 Statistical analysis.....	18
2.3 Results.....	18
2.3.1 Comparison of caffeinated and uncaffeinated results.....	18
Cerebral circulation time (CCT) difference	18
Delay map difference	19
Standard deviation difference.....	21
2.3.2 Neuronal and vascular effects.....	23
2.4 Discussion.....	25
2.4.1 Caffeinated scans gave the faster speed of blood flow	25
2.4.2 Caffeinated scans have lower LFO amplitude.....	26
2.4.3 Possible confounds	27
2.5 Conclusion	27
3. STUDY 2	29
3.1 Introduction.....	29
3.2 Materials and Methods.....	30
3.2.1 Protocol.....	30
3.2.2 Near-infrared Spectroscopy	31

3.2.3	MRI.....	32
3.2.4	Sharp-CO ₂ inhalation (Sharp-CI) task	32
3.2.5	Other induced-hypercapnia tasks.....	32
3.2.6	Data analysis	33
3.3	Materials and Methods.....	34
3.3.1	Sharp-CI results	34
3.3.2	Additional induced-hypercapnia tasks.....	36
3.4	Discussion	40
3.4.1	NIRS signals under sharp-CI task.....	40
3.4.2	Validations	41
3.4.3	Limitations	43
3.5	Conclusion	43
4.	STUDY 3	44
4.1	Introduction.....	44
4.2	Materials and Methods.....	45
4.2.1	Model.....	45
4.2.2	Experimental Design	47
	Structure Scans	47
	EPI Scans.....	48
4.2.3	Data analysis	48
	CSF flow signals	48
	Preprocessing	49
4.2.4	Data and statistical analysis	49
4.3	Results.....	50
4.3.1	CSF flow during wakefulness.....	50
4.3.2	CSF flow signal and <i>ddt</i> (GMS)	51
4.3.3	Spatial-temporal information of the coupling of CSF inflow with the brain signal ..	54
4.4	Discussion	55
4.4.1	Possible driving forces for CSF flow.....	56
4.4.2	Ventricular vs. perivascular effects	59
4.4.3	Sleep vs. awake states.....	59

4.4.4	Limitation and future studies	60
4.5	Conclusion	60
5.	Conclusion	61
REFERENCES	62

LIST OF FIGURES

Figure 2-1 Data processing flowchart. The flowchart presents the procedure of data processing. First, 90 resting-state scans were sorted into caffeinated and uncaffeinated groups. Second, vascular information was extracted from scans separately, which included (a) Time delays between systemic low-frequency oscillations (sLFOs, 0.01–0.1 Hz) of the superior sagittal sinus (SSS) and brain voxels, (b) Cerebral circulation time (CCT) was measured by time delay between sLFOs of SSS and internal carotid artery (ICA), (c) LFOs amplitude in brain voxels were measured. Lastly, the above vascular effect of caffeine was compared with the neuronal effect of caffeine from previous research [45].	16
Figure 2-2 Comparison of time delay distribution between 45 caffeinated RS scans (brown) and 45 uncaffeinated RS scans (gray). Time delays were calculated between (a) superior sagittal sinus (SSS) and global signal (GS), (b) GS and internal carotid artery (ICA), and (c) SSS and ICA. Results with absolute maximum cross-correlation coefficients less than 0.28 were excluded to avoid spurious correlations. Time delay distributions between caffeinated and uncaffeinated scans were compared by Kolmogorov–Smirnov test [45].	19
Figure 2-3 Delay maps. (a) Averaged delay map from 90 RS scans. Time delays were calculated between sLFOs of SSS and all the voxels in the brain. The blue color showed the later arrival time of blood and the blue-lightblue color showed earlier arrival time regarding SSS. (b) The difference between caffeinated and uncaffeinated delay maps. Red-yellow color showed time delays between the voxels and SSS were shorter in the caffeinated scans than the uncaffeinated scans [45].	20
Figure 2-4 Time delay difference and SD difference. Original results of time delay difference (a) and <i>SD</i> difference (b) between caffeinated and uncaffeinated scans were presented as red distribution. Randomization results of time delay difference (a) and <i>SD</i> difference (b) between caffeinated and uncaffeinated scans were presented as blue distribution [45].	21
Figure 2-5 Delay maps and SD maps differences using different threshold method. (a) Thresholded (from randomization) subtraction of delay map (caffeinated – uncaffeinated). (b) Thresholded (from randomization) <i>SD</i> percentage difference ((caffeinated – uncaffeinated) / caffeinated). [45].	21
Figure 2-6 SD map and blood vessel identified in T2- weighted image. Upper panel: Averaged <i>SD</i> map from 90 RS scans. Lower panel: T2- weighted image. Brain region with high systemic low-frequency oscillation amplitude matched the locations of big blood vessels (marked by squares in (b)) [45].	22
Figure 2-7 averaged SD maps and SD intensity profiles. (a1–2) show the average <i>SD</i> maps of caffeinated and uncaffeinated scans at different MNI coordinates. (b1–2) were <i>SD</i> intensity profiles, which reflected the corresponding <i>SD</i> values along the white arrow in both averaged uncaffeinated (gray) and caffeinated scans (brown) from (a1–2), respectively [45].	23
Figure 2-8 Vascular effect of caffeine on 9 RS networks. The significant time delay differences (upper blue panel) and <i>SD</i> differences (lower red panel) between caffeinated and uncaffeinated scans were showed for 9 RS networks. (DMN: default mode network, VIS: visual network, FP:	

frontoparietal network, DA: dorsal attention network, VA: ventral attention network, SAL: salience network, CO: cingulo-opercular network, SM: somatomotor network, AUD: auditory network) [45]. 24

Figure 3-1 Experimental design and setup. Schematic of (a) Configuration of the NIRS channels on the head. (b) Experimental setup of the concurrent fMRI/NIRS experiments (c) the sharp-CI, (d) the long-ramped CI, (e) the BH, and (f) the short-ramped CI tasks. [94]. 31

Figure 3-2 Averaged MCCC from each channel under the sharp-CI task. Averaged MCCC from each channel under the sharp-CI task between $\Delta BOLD\%$ and (a) ΔHbO , (b) ΔHb . Crosses in the channel indicate a p -value larger than 0.05 under the FDR-criterion [94]. 35

Figure 3-3 inconsistent NIRS signal during the sharp-CI task. Results showing inconsistencies in NIRS signals during the sharp-CI task from two example subjects in (a) and (b). The signals of $\Delta P_{ET}CO_2$, $\Delta BOLD\%$, ΔHbO , and ΔHb are shown in the colors of black, purple, red, and blue respectively. The averaged results of ΔHbO and ΔHb are shown at the bottom right of (a) and (b) in red boxes [94]. 35

Figure 3-4 The fMRI and NIRS results from different hypercapnia tasks. The fMRI and NIRS results from the (a) sharp-CI tasks, (b) BH, (c) long-ramped CI, and (d) short-ramped CI. The shaded areas indicate the targeted $\Delta P_{ET}CO_2$ in each task. The averaged $\Delta P_{ET}CO_2$, $\Delta BOLD\%$ (normalized), ΔHbO , and ΔHb signals are shown in columns 1-4, respectively [94]. 37

Figure 3-5 Averaged MCCCs between fMRI and NIRS signals. Averaged MCCCs between $\Delta BOLD\%$ and ΔHbO (ΔHb) signals are shown in column 1 (2). The corresponding tasks are sharp-CI (a), BH (b), long-ramped CI (c), short-ramped CI (d). Crosses in the channel indicate a p -value larger than 0.05 under one-sample t -test [94]. 38

Figure 3-6 The fMRI movie snapshots from one subject under the long-ramped CI task. Three snapshots were captured at (1) rising phase (2) plateau, and (3) falling phase of $\Delta P_{ET}CO_2$ in the long-ramped CI task. During each time point, real-time (a) $\Delta P_{ET}CO_2$ and (b) $\Delta BOLD\%$ (normalized) signals are displayed. Also, $\Delta BOLD\%$ (normalized) maps (red-yellow refers to positive percent changes and blue-light blue refers to negative percent changes) in (c) sagittal, (d) coronal, and (e) axial views are shown. The shaded areas indicate the targeted $\Delta P_{ET}CO_2$ during the task. The black square in every (c) and (e) panel indicate the region of the prefrontal cortex (PFC) [94]. 39

Figure 3-7 Group folding average of signals from the (a) BH and (b) short-ramped CI task. The results of $\Delta BOLD\%$ (normalized), ΔHbO , and ΔHb are showed in columns 1-3, respectively. The time ranged from 0 to 20 second indicates the periods of BH/ramped-increased $\Delta P_{ET}CO_2$ [94]. 42

Figure 4-1 The brain model and its corresponding fMRI signals measured at the fourth ventricle and brain (GMS). (a) The model illustrates the temporal changes in vessel volume with the corresponding effects on the lateral ventricle shape and CSF flow at the fourth ventricle. Blue circles show periods of vessel volume change (i.e., transition). Arrows in the blue circles point to the direction of vessel wall movement. (b) Corresponding signals and their derivatives are observed at the fourth ventricle, brain (GMS). The flow signal is from the inflow ('time of flight') effect. The brain fMRI signal is from the BOLD effect. 47

Figure 4-2 The scan designs and corresponding CSF flow signals. The scan volumes used in the brain scan (a) and the neck scan (b). In the brain scan (a), the signal detected at the first slice (green circle) represents CSF flow into the brain. In the neck scan (b), the signal detected at the first slice (green circle) represents CSF flow into the neck. The corresponding unfiltered, raw time series extracted from the green circles in (a) and (b), are shown in (c) and (d) respectively. They represent CSF flow signals to the brain (c) and to the neck (d). Both show large slow oscillations in addition to rapid oscillations due to cardiac pulsation. (e) Brain segmentation is used to identify gray matter, white matter, and CSF. (f) Blood vessel segmentation in the neck to identify internal jugular veins (IJV). 50

Figure 4-3 The relationships between GMS of the brain, CSF inflow signal (a-c), averaged IJV signal and CSF outflow signal (d-f) from the same research participant. (a) Time series of GMS in purple and its derivatives (*ddt* (GMS)) in red. (b) Time series of filtered *ddt* (GMS) in red with the negative raw CSF inflow signal in blue. It shows CSF inflow signal matches the lower part of filtered *ddt* (GMS). (c) Cross-correlation between filtered *ddt* (GMS) and CSF inflow shows the *ddt* (GMS) is ahead of CSF inflow signal with high MCCC (-0.75). (d) Time series of IJV signal in purple and the derivative of IJV (*ddt* (IJV)) in red. (e) The time series of filtered *ddt* (IJV) in red and CSF outflow signal in blue. It shows CSF outflow signal matches the top part of filtered *ddt* (IJV). (f) Cross-correlation between filtered *ddt* (IJV) and CSF outflow signal shows *ddt* (IJV) is a little behind of CSF outflow signal with high MCCC. GMS: global mean signal. MCCC: maximum cross-correlation coefficient. IJV: internal jugular vein task..... 52

Figure 4-4 The summary of the cross-correlations between CSF inflow signal and *ddt* (GMS) from different regions of interest (ROIs). (a) MCCCs and delays between CSF inflow signal and *ddt* (gray matter), *ddt* (white matter), *ddt* (CSF) in each participant and the averaged result from all participants. All the *ddt* (GMS) in different ROIs are temporally ahead of CSF inflow signal with high negative MCCC. (b) Averaged MCCC and delays between CSF outflow signal and *ddt* (IJV). All but one have high positive MCCC and positive delays. GMS: global mean signal. MCCC: maximum cross-correlation coefficient. IJV: internal jugular vein. 53

Figure 4-5 Group average of voxel-wise cross-correlation between *ddt* (fMRI signal) and CSF inflow signal. (a-b) Various views of whole-brain MCCC show that most of the *ddt* (fMRI signal) in the brain were negatively (red-yellow) correlated with CSF inflow signal. (c) The distribution of MCCC. (d-e) Various views of whole-brain delays show that most of the *ddt* (fMRI signal) is ahead of CSF inflow signal. (f) The distribution of the delays. MCCC: maximum cross-correlation coefficient. 55

Figure 4-6 (a) The model depicts the low-frequency (e.g., vasomotion) and high-frequency (heartbeat) vessel volume changes and their impacts on the fMRI, and CSF inflow signals. (b) CSF inflow signal (upper panel: raw data of CSF inflow; lower panel: high pass filtered CSF inflow (>0.6Hz) to extract the heartbeat signal). Three red circles represent big drops of CSF inflow, which indicate CSF outflow or no flow. In these periods, smaller amplitudes of heartbeat signals are found (pointed by red arrows). (c) High-frequency CSF inflow signal (>0.6Hz, blue) and heartbeat signal recovered from the brain data using “Happy” (Aslan et al., 2019). (d) Power spectrum (arbitrary unit) of CSF inflow signal (left) and power spectrum of heartbeat signal (right). These two panels show that 1) the heartbeat signal can be detected in CSF inflow signal, which matched that of the brain; 2) little or no delay was found in the heartbeat signal in the brain and that detected in CSF inflow..... 56

Figure 4-7 CSF net flow assessment. (a) Net flow measurements for CSF inflow (red) and outflow (blue) from one participant. (b) Net flow difference for all participants. 58

ABSTRACT

The human brain is sensitive to stimuli from the outside world. Those stimuli could induce physiological and neuronal reactions in the brain (e.g. neuron firing and blood flow changes). Those reactions can be measured by several neuroimaging modalities and recorded as physiological and neuronal signals. Interestingly, current studies tend to remove the physiological signal from the brain (e.g., respiration) to focus on the neuronal signal. However, physiological signals in the brain contain some useful information. For example, previous research showed that the averaged signal in the brain, which was commonly removed as physiological noise, can track cerebral blood flow (CBF). Also, by giving physiological stimuli, we can expose hidden deficits in the brain in some cases. Therefore, understanding both physiological signals in the brain and physiological effects on the brain is important. The goal of my study is to investigate physiological signal characterizes various physiological stimuli in the brain using multimodal imaging. Functional magnetic resonance imaging (fMRI) and near-infrared spectroscopy (NIRS) were applied in the following studies. In the first study, the physiological parameters were exploited from fMRI scans, which were recorded after a person drinking coffee. The results derived from fMRI scans illustrated that caffeine decreases the blood vessels' size and increased the blood flow speed in blood vessels in the brain. In the second study, vasoactive stress tests (i.e., hypercapnia, the elevated partial pressure of arterial CO_2 (PaCO_2)) were introduced as a dominant physiological stimulus (caused an increase of CBF) and measured by fMRI and NIRS concurrently. The results indicated that the cerebral and extracerebral reactivity to elevated PaCO_2 depended on the rate of the CO_2 increase. Later, my third study comparing hyperoxia (elevated partial pressure of arterial O_2 (PaO_2)) and hypercapnia effects on the brain measured by fMRI and NIRS. Since NIRS measured both oxy- and deoxy- hemoglobin concentrations, NIRS signals have advantages to differentiate hypercapnia and hyperoxia effects on the brain compared to fMRI. To further understand physiological signals in the brain, coupling between hemodynamic and the inflow effect of CSF dynamic was investigated using fMRI in my fourth study.

1. BACKGROUND

The human brain is sensitive to stimuli from the outside world (e.g., visual, auditory gas, drug stimuli) [1-4]. Those stimuli could have both physiological and neuronal effects on the brain and are crucial for brain health. Those brain reactions to those stimuli can be recorded as physiological and neuronal signals using several neuroimaging modalities. For example, propofol, an anesthetic drug used to induce anesthesia (reduced consciousness), can decrease cerebral blood flow [5, 6]. Under the administration of propofol, the changing brain networks (signals correlations in the brain) were significantly correlated with regional CBF changes under anesthesia by propofol [7]. Interestingly, current studies tend to treat physiological signals (e.g., respiration, heartbeat) as noise and remove them from the brain to focus on neuronal signals [8-12]. For example, the global signal (mean time series calculated within the brain) is removed as a preprocessing step since it is contributed by various noise components [13, 14]. However, a previous study found that there was some useful physiological information can be extracted from those physiological noises. [15-18]. For example, a previous study showed that the low-frequency oscillations (LFOs, 0.1-0.01Hz) propagated through the brain like the cerebral circulatory system [15]. Moreover, the following study demonstrated that the patterns of propagating LFOs represent cerebral blood flow, which was validated by dynamic susceptibility contrast (DSC) magnetic resonance imaging (MRI) scans (i.e., bolus tracking) [18]. Furthermore, by giving physiological stimuli, we can expose hidden deficits in the brain. For example, a previous study showed regions with brain diseases can be detected by CO₂-induced cerebral blood flow increases [19]. Therefore, it is important to understand those physiological signals and their effects on the brain. To fulfill this goal, my studies focus on the physiological stimuli that can induce a physiological effect on the brain and detect those effects by motional modalities.

2. STUDY 1

This chapter is reproduced with copyright permission from Journal of neuroscience research, 2019. 97(4): p. 456-466. doi: 10.1002/jnr.24360 [20].

2.1 Introduction

Blood-oxygen-level-dependent (BOLD) contrast in functional MRI (fMRI) has been widely applied to investigate brain activity [21, 22]. However, BOLD fMRI does not measure neuronal activation directly. It reflects neuronal activation through neurovascular coupling. In addition to neuronal activity, physiological processes which make alterations in cerebral blood flow (CBF), cerebral blood volume (CBV), and cerebral blood oxygen consumption (CMRO₂) can also affect BOLD signals [23-25]. Thus, some features of BOLD signals can be used to assess systemic physiology. This additional physiological information does not require extra scans. More importantly, it can offer concurrent and complement physiological information to neuronal activation. The combined information can shed light on the interactions between neuronal activation and non-neuronal physiological processes.

Among all the features of resting-state (RS) BOLD signals, it has been demonstrated that the time delay and amplitude of low-frequency fluctuations (ALFFs) can be used to assess the cerebral blood velocity and cerebral blood density respectively [15, 26]. In RS BOLD signals, systemic low-frequency oscillations (sLFOs) are the physiological RS BOLD signals with the frequency range from 0.01 to 0.1Hz, which overlaps with the frequency range of RS BOLD signals (i.e. neuronal). However, the RS BOLD signals are more regional, leading to different RS networks with corresponding RS BOLD signals. On the other hand, sLFOs were traveling global signals with likely extracerebral origins [27], which might be related to CO₂ fluctuation in the blood, vasomotion, Mayer wave, etc [11, 28, 29]. The reason that they are called “systemic” is that the same sLFOs, which are found in RS BOLD signals in the brain (especially large veins), can be detected concurrently by optical method at peripheral sites (fingertip and toe) as slow changes in oxy- and deoxyhemoglobin concentration with time delays [30]. This study demonstrated that the sLFO is a blood-borne oscillation that travels to various parts of the body with blood. Recently, we were able to identify these sLFOs in large arteries and veins (i.e. the internal carotid artery

(ICA), superior sagittal sinus (SSS), and internal jugular vein) in the neck from the resting state (RS) Myconnectome data [31]. Time delays of approximately 7 seconds were found between these two highly correlated signals, which is consistent with the cerebral circulation time (CCT) normally measured by ultrasound [32]. Another feature is ALFFs (i.e. standard deviation (SD)), which also provide physiological cerebral vascular properties, such as cerebral blood volume, vascular density, etc. The ALFFs have been shown to contain a vascular component related to the hypercapnic index [33]. Vigneau-Roy et al. 2014 illustrated that the ALFFs of RS BOLD signals were related to vascular density [26]. The LFO amplitude has also been used to indicate vasoconstriction [34].

Caffeine, as an adenosine A2 receptor antagonist, has both neuronal and cerebral vascular effects. For neuronal effects, it is well-known that caffeine can increase the alertness level [35]. It has also been found that brain response to visual stimulation is faster after ingestion of caffeine [36-38]. Many studies on caffeine effects in the brain focus on these neuronal activities, e.g. investigating brain network connectivity [34, 39, 40]. However, caffeine also has profound vascular effects. After 250 mg caffeine intake, the resulting vasoconstriction can decrease the Cerebral BF by about 27% [41-43]. These global vascular effects can also alter brain activity. So far, few functional MRI (fMRI) studies have sought to understand caffeine’s vascular effect on resting-state (RS) fMRI, and more importantly, understand the interaction with neuronal activations. In this work, we will study the vascular effects of caffeine by accessing 1) blood arrival time, 2) cerebral circulation time (CCT), and 3) blood density in RS fMRI scans. The results will be compared with those from brain network analyses (published separately) and paint a thorough picture of the effects of caffeine.

2.2 Method

2.2.1 Data selection

The publicly available Myconnectome dataset (<http://myconnectome.org/wp>) was chosen to investigate the cerebral vascular effects of caffeine. This dataset is about a two-year study of an individual subject (Male, aged 45). There are several advantages to using this dataset: (1) the Myconnectome dataset recruited only one single subject, which eliminates between-subject variation. (2) The data contains 90 high-quality resting-state fMRI scans, with an equal number of

caffeinated scans (scans were taken 90 minutes after caffeine ingestion) and un-caffeinated scans (i.e. 45 each). (3) Structural images included T1 and T2 weighted scans with high spatial resolution, which made the identification of large blood vessels (arteries and veins) easier.

2.2.2 Image acquisition

Detailed scan parameters can be found in Poldrack et. al 2015. In short, most of the 10-minute resting-state fMRI scans with eyes closed were acquired using multi-band EPI sequence (TR=1.16 s, TE=30 ms, flip angle=63 degrees (the Ernst angle for the grey matter), voxel size= $2.4 \times 2.4 \times 2$ mm, distance factor=20(percentage sign), 68 slices, oriented 30 degrees back from AC/PC, 96×96 matrices, 230 mm FOV, MB factor=4, 10:00 scan length) [44].

2.2.3 Data processing

Figure 2-1 shows the flow chart of data processing. Data were processed using FSL (FMRIB Expert Analysis Tool, v6.01, <http://www.fmrib.ox.ac.uk/fsl>, Oxford University, UK [45]) and a locally developed program (MATLAB 2017a, The MathWorks Inc., Natick, MA, 2000). RS fMRI scans were preprocessed with the following steps recommended by Power et al., 2014. This included: 1) motion correction (FSL mcflirt), 2) linear detrending (MATLAB detrend; 'linear'), 3) Nuisance signals removal (six motion parameters and their derivatives estimated by mcflirt) using a general linear model (FSL fsl_glm), 4) spatial smoothing with a Full-Width Half-Maximum of 5mm isotropic Gaussian kernel [14].

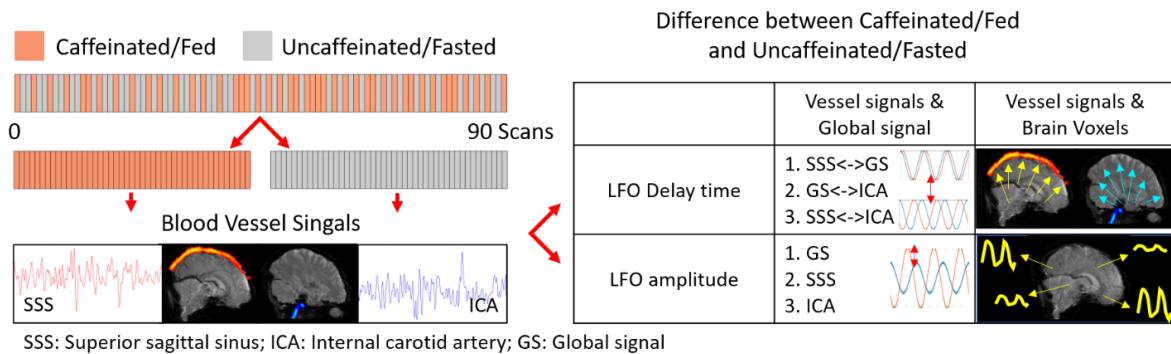


Figure 2-1 Data processing flowchart. The flowchart presents the procedure of data processing. First, 90 resting-state scans were sorted into caffeinated and uncaffeinated groups. Second, vascular information was extracted from scans separately, which included (a) Time delays between systemic low-frequency oscillations (sLFOs, 0.01–0.1 Hz) of the superior sagittal sinus (SSS) and brain voxels, (b) Cerebral circulation time (CCT) was measured by time delay between sLFOs of SSS and internal carotid artery (ICA), (c) LFOs amplitude in brain voxels were measured. Lastly, the above vascular effect of caffeine was compared with the neuronal effect of caffeine from previous research [20].

2.2.4 Vascular measures

We assessed the caffeinated/uncaffeinated difference in the following parameters: 1) CCT from the time delays between sLFOs in fMRI signals from ICA and SSS; 2) delay maps (i.e. cerebral blood arrival map) obtained by calculating the voxel-wise time delays between sLFOs in fMRI signals from each voxel and SSS; 3) cerebral blood density from the voxel-wise SDs of LFO in fMRI signals. Lastly, we compared our results with previous research of RS network connectivity on the same dataset [44].

2.2.5 Cerebral circulation

To calculate the delays of the sLFOs between ICA and SSS in caffeinated and uncaffeinated scans, we applied the same method in Tong et al. 2018 to extract the fMRI signals in these large blood vessels. In short, left and right ICAs and SSS were identified from structural images (T1- and T2- weighted images) [31]. Time series within these identified blood vessels were extracted and averaged (FSL fslmeants) from the RS fMRI (after registering high-resolution vessel masks onto the low-resolution fMRI images). To calculate the time delays between the sLFOs of two vessels, we conducted the following steps. 1) A band-pass zero-lag Butterworth filter (0.01-0.1Hz) was applied to the time series from SSS, global signal (GS), and ICA to extract the sLFOs, which were then oversampled to increase the temporal resolution (from 1.16s to 0.116 s). 2) The principal component analysis was then applied to the signals from left and right ICAs to obtain the principal signal of the low-frequency component to improve the signal-to-noise ratio. 3) Time delays between the sLFOs from GS, ICA, and SSS were calculated using cross-correlation (xcorr in Matlab), which found the absolute maximum cross-correlation coefficient (MCCC) between the signals within a ± 15 s window. The MCCC threshold was set at 0.28, which was the significance threshold based on previous research [27]. In addition, voxel-wise delay maps were generated based on the method developed previously [46]. In short, the time delay between every voxel's RS BOLD signal and the SSS signal was calculated to represent the blood arrival time at that voxel. The delays calculated between large vessels, as well as the whole brain delay maps, were later compared between caffeinated and uncaffeinated scans to expose the caffeine effects on the circulation.

2.2.6 Cerebral blood density (volume)

Previous research reported that the ALFFs in the RS BOLD signal was positively correlated with blood density in the voxel [26]. Here, we calculated the SD in RS BOLD signal to represent the cerebral blood density (volume). Voxel-wise SD maps were calculated with the following steps: First, a band-pass zero-lag Butterworth filter (0.01-0.1Hz) was applied to the time series of each voxel in the brain. Second, SDs of the low-frequency time series were calculated in each voxel. Finally, the SD differences (in percentage) between caffeinated and uncaffeinated scans were obtained by subtraction.

2.2.7 Statistical analysis

The distribution differences of time delays between GS, ICA, and SSS in caffeinated and uncaffeinated scans were tested by the Kolmogorov–Smirnov test [47].

To assess the statistical significance of the difference between caffeinated and uncaffeinated scans, we conducted the randomization procedure. In detail, 90 delay maps (or SD maps) were randomly placed into two groups (45 each). Each group would have roughly the same numbers of caffeinated scans as well as uncaffeinated scans. The averaged delay maps (or SD maps) were calculated from each group and the subtraction between these two groups was obtained. Since there is no difference in the subtraction (because equal numbers of caffeinated and uncaffeinated scans are included in each group), the subtraction result should be close to 0 and its distribution could be used to extract the threshold of the null hypothesis to assess the real effect. The processes of generating random groups and the subtraction between these groups were repeated for 10000 trials. The threshold was selected as $P < 0.01$ or $P > 0.99$ (P indicated the probability of having spurious results), from the averaged distribution of the subtractions.

2.3 Results

2.3.1 Comparison of caffeinated and uncaffeinated results

Cerebral circulation time (CCT) difference

Figure 2-2 shows the time delay differences between SSS and GS, GS and ICA, ICA and GS. Time delays are significantly shorter between SSS and ICA in the caffeinated scans ($5.03 \pm 0.617s$) than those from the uncaffeinated scans ($5.96 \pm 0.659s$) ($p < 0.001$), indicating the shorter CCTs in

caffeinated scans. This result is consistent with the following observations: 1) time delays are significantly shorter between SSS and GS in the caffeinated scans ($2.15 \pm 0.237s$) than the uncaffeinated scans ($2.74 \pm 0.303s$) ($p < 0.001$). 2) time delays are significantly shorter between GS and ICA in caffeinated scans ($2.87 \pm 0.767s$) than uncaffeinated scans ($3.38 \pm 0.783s$) ($p < 0.05$).

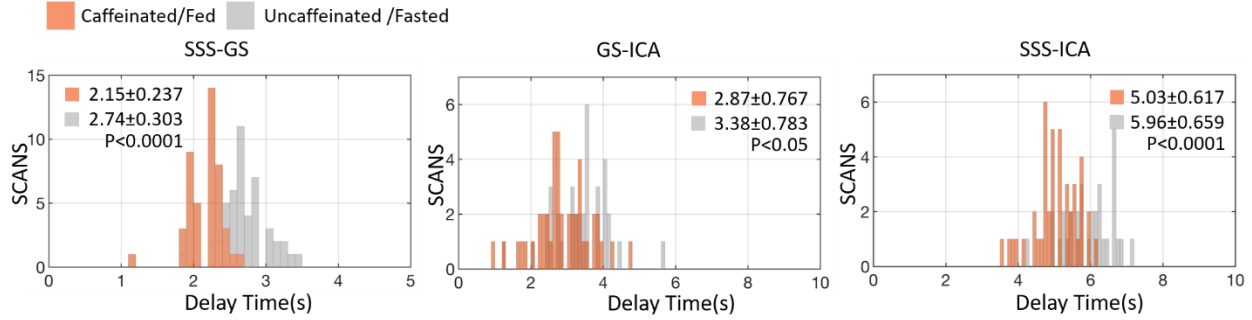


Figure 2-2 Comparison of time delay distribution between 45 caffeinated RS scans (brown) and 45 uncaffeinated RS scans (gray). Time delays were calculated between (a) superior sagittal sinus (SSS) and global signal (GS), (b) GS and internal carotid artery (ICA), and (c) SSS and ICA. Results with absolute maximum cross-correlation coefficients less than 0.28 were excluded to avoid spurious correlations. Time delay distributions between caffeinated and uncaffeinated scans were compared by Kolmogorov–Smirnov test [20].

Delay map difference

Figure 2-3 (a) shows the average delay map from 90 RS scans (from a single subject). It demonstrates that the delay map calculated from this data largely matches the cerebral blood circulation. Red indicates the early arrival of the sLFOs (i.e. blood), while blue denotes late arrival. Since the voxel-wise delay value was calculated between the sLFO from each voxel and the SSS, the arrival times were relevant to that of SSS. Figure 2-3 (a) shows that the brain is dominated by “Blue”, indicating that blood reached most of the voxels before it arrived at SSS (which is expected, as the SSS is a major blood drainage vessel from the brain). Interestingly, the ICAs were automatically identified as the regions where blood arrives very early (see the arrows in figure 2-3 (a)). This phenomenon confirmed that sLFOs indeed were “pumped” into the brain through arteries, such as ICAs. A detailed discussion about the sLFOs in ICA can be found in our previous publication [31]. The fact that the delay map can automatically locate ICA out of RS fMRI data with correct delay values showed the robustness of the sLFO in fMRI signal as well as our method. Delay map difference obtained by subtracting the delay map of 45 caffeinated scans from that of 45 uncaffeinated scans is shown in figure 2-3 (b). It shows that the subtracting result of the delay

maps is dominated by “Red”, indicating that blood flow speed increased in most of the brain regions under the effect of caffeine.

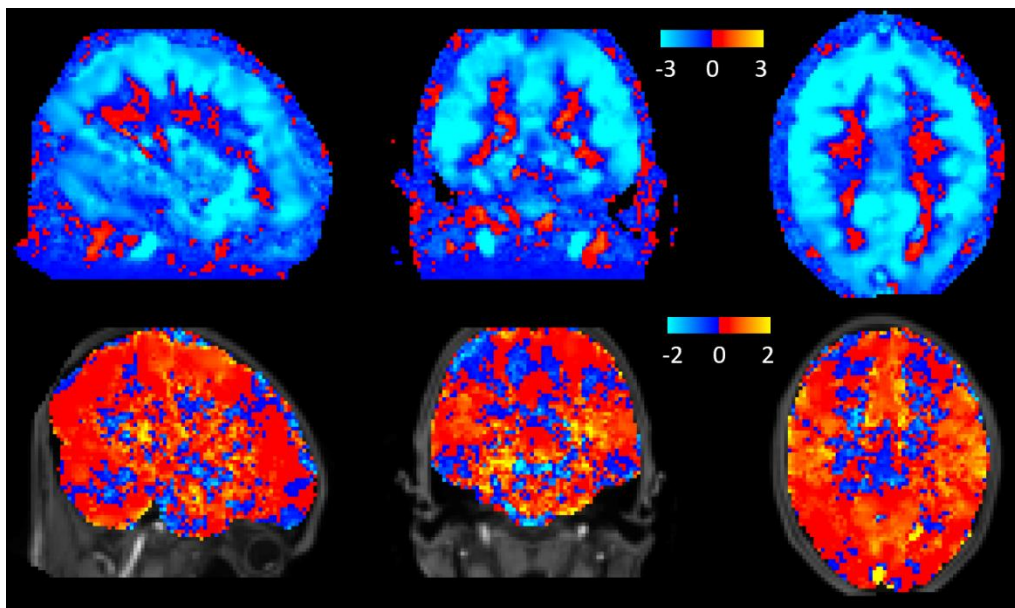


Figure 2-3 Delay maps. (a) Averaged delay map from 90 RS scans. Time delays were calculated between sLFOs of SSS and all the voxels in the brain. The blue color showed the later arrival time of blood and the blue-lightblue color showed earlier arrival time regarding SSS. (b) The difference between caffeinated and uncaffeinated delay maps. Red-yellow color showed time delays between the voxels and SSS were shorter in the caffeinated scans than the uncaffeinated scans [20].

Figure 2-4 (a) shows the distribution of randomized subtraction (from 10000 random combinations) in blue and the real caffeinated vs. uncaffeinated subtraction in red (see 2.4.3). From the distribution of randomized subtraction in figure 2-4 (a), we found the results were clustered tightly around 0, which was expected due to no caffeine effects in the randomized data. However, the distribution of real caffeinated vs. uncaffeinated subtraction was much broader. This further indicates that the differences calculated between caffeinated and uncaffeinated scans are significant. We obtained the thresholds on delay differences to be $> 0.037s$ or $< -0.042s$ ($P < 0.01$), which were used on figure 2-5 (a) and the upper panel of figure 2-8 to produce statistically significant delay maps differences.

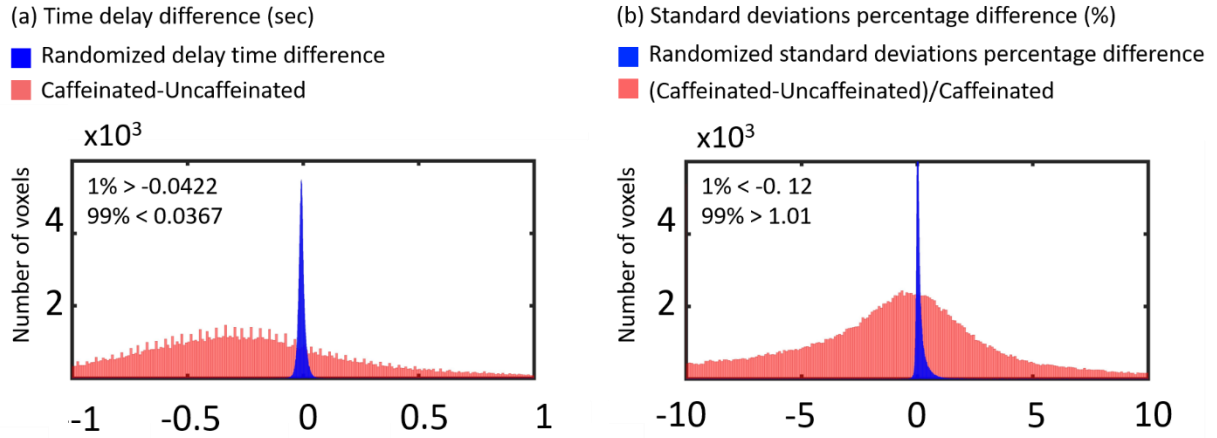


Figure 2-4 Time delay difference and SD difference. Original results of time delay difference (a) and *SD* difference (b) between caffeinated and uncaffeinated scans were presented as red distribution. Randomization results of time delay difference (a) and *SD* difference (b) between caffeinated and uncaffeinated scans were presented as blue distribution [20].

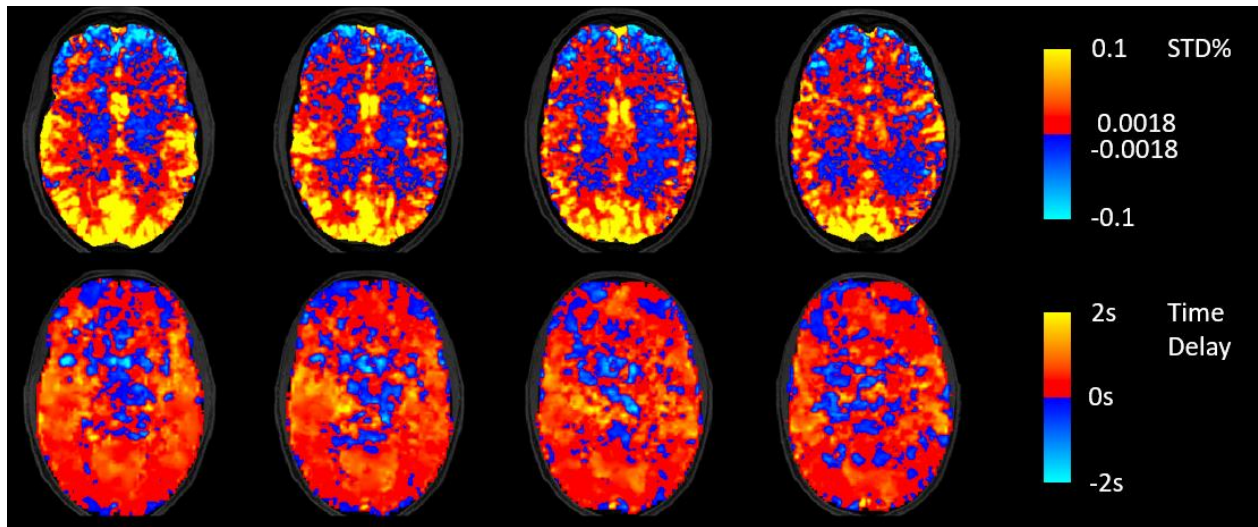


Figure 2-5 Delay maps and SD maps differences using different threshold method. (a) Thresholded (from randomization) subtraction of delay map (caffeinated – uncaffeinated). (b) Thresholded (from randomization) *SD* percentage difference ((caffeinated – uncaffeinated) / caffeinated) [20].

Standard deviation difference

Figure 2-6 (a) shows that voxels with higher LFO amplitude (i.e. *SD*) in yellow, projected onto the subject's own structural scan (T2-weighted image). The yellow regions overlapped precisely with the visible blood vessels (marked by squares in T2-weighted image figure 2-6 (b)). This is in accordance with the findings in Vigneau-Roy et al. 2014, which reported that the ALFFs of RS BOLD signal was positively correlated with blood density in the voxel [26].

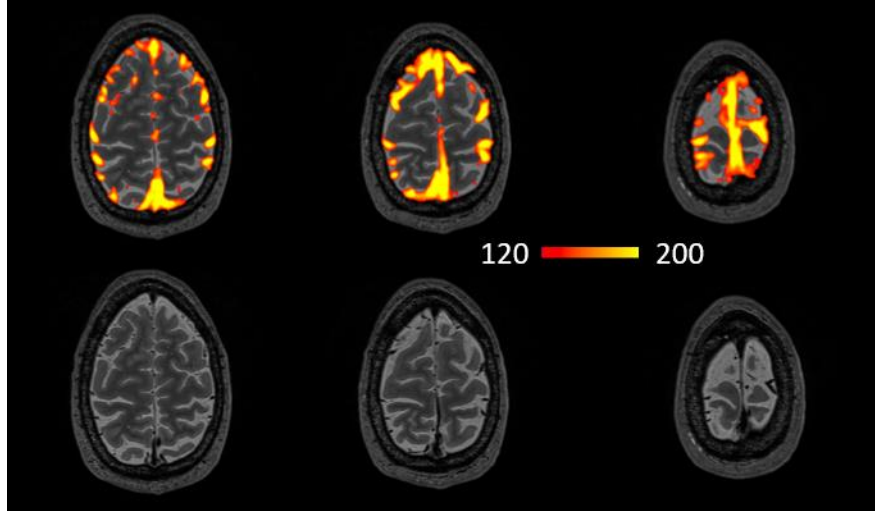


Figure 2-6 SD map and blood vessel identified in T2- weighted image. Upper panel: Averaged *SD* map from 90 RS scans. Lower panel: T2- weighted image. Brain region with high systemic low-frequency oscillation amplitude matched the locations of big blood vessels (marked by squares in (b)) [20].

We used this feature to assess blood vessel changes due to the caffeine effect. The rows/columns of voxels (shown by arrows) in figure 2-7 (a1-a2) pass through areas with high blood density (or large blood vessels). The corresponding profile (of RS BOLD signals' SDs along the white arrow) is shown in figure 2-7 (b1-b2), which presented the averaged results of uncaffeinated scans and caffeinated scans. From figure 2-7 (a1-a2), visible decreases in the yellow pattern were found in caffeinated results, which is confirmed by figure 2-7 (b1-b2). It shows the intensity profile of the SDs of LFOs was “constricted” and decreased after coffee. This observation could be interpreted as vasoconstriction due to the caffeine. To assess the vessel constriction effect in the whole brain, we compared the SD difference in percentage ($((\text{caffeinate} - \text{uncaffeinated}) / (\text{caffeinated}))$) between caffeinated and uncaffeinated scans. To assess the result from the statistical point of view, we also conducted the “randomization” procedure used before, with similar findings (shown in figure 2-4 (b)). The distribution of real caffeinated vs. uncaffeinated subtraction was much broader than the results from randomized subtractions, indicating the difference calculated between caffeinated vs. uncaffeinated is not spurious but robust. We obtained the thresholds on percentage SD difference to be $> 1.01\%$ or $< -0.12\%$ ($P < 0.01$), which were applied on figure 2-5 (b) and the lower panel of figure 2-8 to produce the map of statistically significant SD differences.

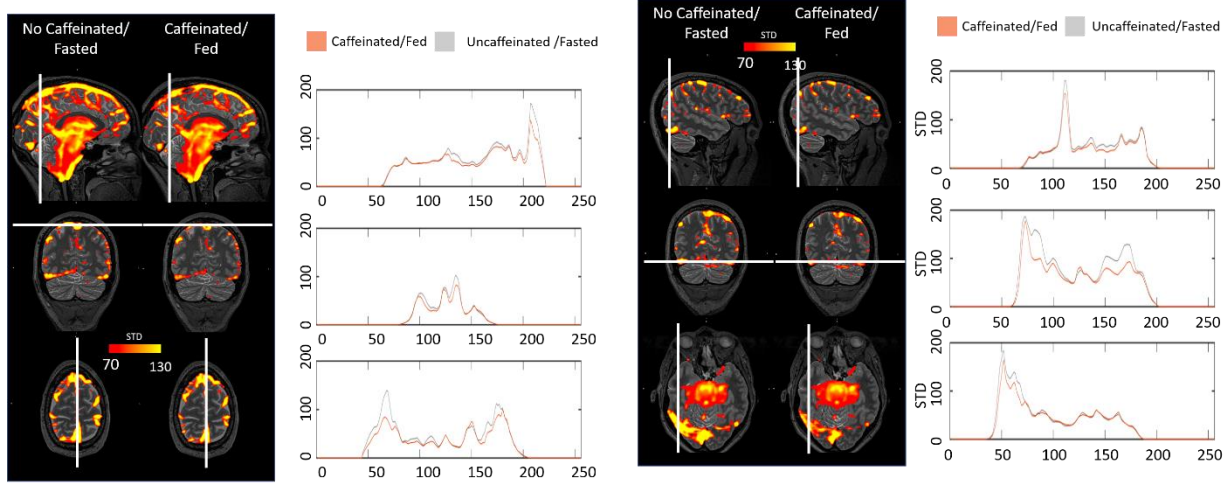


Figure 2-7 averaged SD maps and SD intensity profiles. (a1–2) show the average *SD* maps of caffeinated and uncaffeinated scans at different MNI coordinates. (b1–2) were *SD* intensity profiles, which reflected the corresponding *SD* values along the white arrow in both averaged uncaffeinated (gray) and caffeinated scans (brown) from (a1–2), respectively [20].

2.3.2 Neuronal and vascular effects

As we know, caffeine has both vascular and neural effects. It is of great interest to understand the spatial correlation between vascular and neuronal effect (from previous studies). In detail, we conducted the following steps: First, significant whole-brain time delay differences (Figure 2-5 (a)) and SD percentage differences (Figure 2-5 (b)) were parcellated according to nine functionally coherent RS networks [48]. These well-known RS networks have been studied with the Myconnectome dataset previously to assess the neuronal effect of caffeine [44, 49]. Subsequently, the average of time delay differences and SD percentage differences were obtained from each network. The results were shown in figure 2-8. Negative values of the blue boxplot indicated shorter time delays, while negative values of the red boxplot showed a smaller vessel size after caffeine intake.

In figure 2-8, significantly shorter time delays and smaller SDs can be found in all nine RS networks in caffeinated scans. The top four RS networks with the highest time delay differences (i.e. auditory, somatomotor, visual and, ventral attention networks), are also the top four networks with the highest SD percentage differences. Moreover, we found high linear correlations between relative fluctuations (represented by black dotted linked by solid lines in figure 2-8.) in averaged differences of time delays and SDs among different networks ($r= 0.6$, $p= 0.09$, high p -value

reflected few data points). This feature indicates that network-specific flow velocity changes are well correlated with the vessel size changes under the influence of caffeine.

Interestingly, Poldrack et al. found significantly lower connectivity within and between somatomotor, dorsal attention, and visual networks in caffeinated scans. Moreover, similar decreasing connectivity was found within the motor cortex after caffeine intake [34]. These RS networks (i.e. motor, visual) with decreasing connectivity were the same networks that have the largest time delays and SDs changes after caffeine intake (except dorsal attention network). It shows that caffeine has profound vascular effects (e.g. vessel constriction) in the brain regions where neuronal connectivities were also weakened. This is the first study to expose simultaneously the vascular and neuronal effect of a drug from the same resting-state fMRI data. The interaction between regional perfusion and neuronal activity, exposed by the method, is crucial for the understanding of the effects of drugs, brain diseases, etc. More qualitative studies of large populations are needed to fully explore the effects.

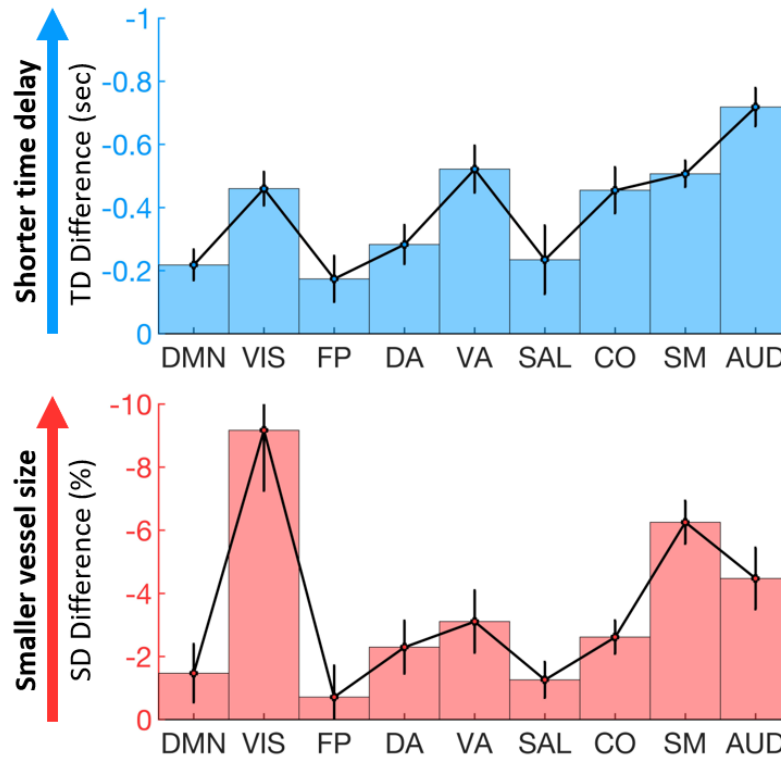


Figure 2-8 Vascular effect of caffeine on 9 RS networks. The significant time delay differences (upper blue panel) and *SD* differences (lower red panel) between caffeinated and uncaffeinated scans were showed for 9 RS networks. (DMN: default mode network, VIS: visual network, FP: frontoparietal network, DA: dorsal attention network, VA: ventral attention network, SAL: salience network, CO: cingulo-opercular network, SM: somatomotor network, AUD: auditory network) [20].

2.4 Discussion

2.4.1 Caffeinated scans gave the faster speed of blood flow

Figure 2-2 showed statistically significant shorter time delays of sLFOs between SSS and ICA, in caffeinated scans than in uncaffeinated scans (~0.9s), which could be interpreted as decreases of CCTs. However, studies from positron emission tomography (PET) and arterial spin labeling (ASL) reported that decreasing CBF was detected after caffeine ingestion [34, 42, 50, 51]. Decreasing CBF would, on the surface, seem to imply an increase of the CCT. This seems to contradict the finding in this study. One possible explanation may lay in the fact that CCT is not necessarily inversely correlated with CBF. CCT reflects the time for a bolus or red blood cells to travel from the ICA to the SSS (speed). However, CBF is measured in the amount of blood (ml) passing through a certain mass of tissue (100g) in unit time (e.g. min). If vessel size stays the same, an increase in CBF will decrease CCT. However, in the situation of caffeine, pressure-induced by vessels constriction (coupled with elevated cerebral blood [52]) leads to the increased blood flow speed (see section 4.2 in the discussion). However, the effects of vessel constriction on CBF are twofold: 1) elevated blood speed will increase CBF; 2) vessel constriction will decrease CBF. Since the latter effect is dominant ($\sim r^2$, r is vessel diameter), vessel constriction will lead to a decrease in CBF. This model explains how caffeine-related vessel constriction can increase the blood flow speed inside the vessels, (leading to shorter CCT) while decreasing the CBF. Nevertheless, a caffeine study using transcranial Doppler to measure the velocity of the middle cerebral artery (MCA) after 250mg of caffeine ingestion showed a significant reduction of the velocity by 13% and reduction of MCA diameter by 4.3% [53]. This does not contradict our model (see in next paragraph) since the RS BOLD signals we studied (e.g. SSS and global mean) are mostly vein signals. The perfusion parameters we derived, including time delay and SD, are biased/more sensitive towards the venules and veins. Therefore, we think the velocity change and vessel constriction measured by RS BOLD signals mostly happen in the capillary, venules, and veins (see discussion in 4.3).

Delay map differences between uncaffeinated scans and caffeinated scans are shown in figure 2-5 (a). The regions in blue-light blue are the areas where the time delays are shortened referred to as SSS (i.e. increase cerebral blood flow speed). Figure 2-5 (a) showed that in most of the brain the cerebral blood flow speed did increase mildly (within 1s) after caffeine intake. However, there are also regions where CBF speed is reduced (red-yellow regions: longer time

delays referred to SSS, especially in figure 2-5 (a)). These regions are concentrated in the lower part of the brain overlapping with MCA. This observation matched the previous publication of transcranial doppler studies of caffeine [53].

2.4.2 Caffeinated scans have lower LFO amplitude

It has been known that areas of high SDs in RS fMRI correspond very well with large vessels in the flow-weighted image [54]. It was even suggested to use these SD maps to identify the location of large vessels. A recent study has investigated the link between regional variations of vascular density (VAD) and the ALFFs of RS BOLD signals. They found a positive correlation between the VAD (from the venous vascular tree in susceptibility-weighted imaging) and the ALFFs. These findings were similar to the results shown in figure 2-6. As result, vessel constriction will decrease the VAD signal, which results in smaller ALFFs. We can see in figure 2-7 that the SD profile curves are narrower and shorter in the caffeinated scans, which indicated that the effect of caffeine is largely vessel constriction. This is more obvious in the case of large veins. In the top left graphs of figure 2-7, SSS were identified with RS BOLD signals of high SD. Its diameter became smaller after caffeine intake. The profile curves (shown on the right) confirmed the observation, which was consistent with the previous findings of the reduction of BOLD amplitude after caffeine intake [34, 55]). Moreover, a similar effect was also found in the global LFO [51]. To validate the global effect of caffeine, the SD of global LFO was also calculated in this study. The result indicated that the SDs of LFOs were significantly larger in uncaffeinated scans than in caffeinated states ($p < 0.001$), which was consistent with previous findings [51].

The whole-brain SD difference between uncaffeinated scans and caffeinated scans was shown in figure 2-5 (b). Red-yellow regions indicated the vessel constriction after caffeine intake, while the blue-light-blue regions showed the opposite effects. We can see that vessel constrictions are commonly found in the regions of high blood density (e.g. gray matter), while the opposite was found in the white matter and lower part of the brain. Our results are consistent with previous ASL findings, which reported that decreasing CBF was widespread in the grey matter after caffeine intake [56, 57]. Compared to the delay map difference shown in figure 2-5 (a), we found that the regions of vessel constriction after caffeine intake overlap largely with the regions where the blood

flow speed increases. This result is consistent with our model proposed in 2.4.1. In 2.4.3, we will further discuss the spatial correlations of these two vascular effects.

2.4.3 Possible confounds

In this study, we want to understand the effects of caffeine on vasculature. However, there are three limitations. First, our study was on a single subject. The studies with more subjects are needed to validate the findings. Second, in the original Myconnectome study, for the scans that subject drank the coffee previously, he also had breakfast. For those scans the subject did not drink coffee, the subject did not have breakfast (for the reason of blood draw). Therefore, there is a risk that our results are confounded with the effect of food intake. These confounding effects include calorie intake, salt intake, etc. However, it was found that food intake made no significant changes in arterial blood pressure, CBF, or cerebral oxygen consumption [58]. Thus, we believe that our findings were largely caused by the vasoconstriction effect of caffeine. In our future studies, we will eliminate these confounding effects.

A second confound is that the subject reported that there was a 90-minute lapse (from the private email exchange with the author) between the coffee-drinking and the scan. This might be considered too long for the caffeine effect to be sustained. However, researchers have found that profound caffeine effects are still detectable 90 minutes after caffeine intake [41].

Finally, the amount of caffeine intake before caffeinated scans was 2 shots of espresso (from the private email exchange with the author). According to previous research, 2 shots of espresso contain roughly 140 mg caffeine [59]. We were concerned about the moderate amount (~140 mg) of caffeine consumed in this study. However, other studies have shown that relative MR flow signals decreases were similar between 100 mg and 200 mg caffeine intake [60]. Therefore, we believe that the main effect we studied is from caffeine.

2.5 Conclusion

To the best of our knowledge, this is the first study using dynamic features of sLFOs to extract physiological perfusion information from RS fMRI drug studies (i.e. caffeine). We have illustrated that caffeine decreases the vessel size (i.e. the lower dynamic SD of LFO) and increased the blood flow speed in those vessels (i.e. the shorter time delays), using only fMRI data. These

findings were supported by the spatial overlapping of these two vasoconstriction effects of caffeine. Furthermore, we found these vascular effects are also spatially correlated with the neuronal effect of caffeine obtained from previous studies. In conclusion, we demonstrate that vascular features can be extracted from fMRI data which may offer valuable complementary information to the neuronal activation. This is extremely useful in drug studies, where vascular and neuronal effects are intertwined, and understanding the individual effect as well as the interactions is crucial. In the future, we will apply our method to assess the vascular information from drug-related fMRI studies and compared it with the neuronal activations quantitatively.

3. STUDY 2

This chapter is reproduced with copyright permission from Journal of Biophotonics, 2020. 13(11): p. e202000173. doi: 10.1002/jbio.202000173 [61].

3.1 Introduction

Additional to caffeine, hypercapnia, a condition where CO_2 is elevated, is known to cause a global increase in CBF due to the potent effect of CO_2 as a vasodilator [62]. Vasoactive stress tests (i.e. hypercapnia, elevated partial pressure of arterial CO_2 (PaCO_2)) are widely used in imaging studies to expose hidden brain perfusion deficits by increasing cerebral blood flow (CBF) [23, 63, 64]. Increasing PaCO_2 decreases pH and relaxes vascular smooth muscle cells in arteries, ultimately leading to an increase in CBF [65, 66]. The end-tidal CO_2 (P_{ETCO_2} : the concentration of CO_2 at the end of exhaled breath) is commonly used as a surrogate signal for PaCO_2 [23, 63, 64, 67, 68].

There are two common methods used to induce hypercapnia. The first method is CO_2 inhalation, which requires a subject to wear a breathing mask that is connected to a system that controls the mixture and flow rates of gases (e.g. O_2 , N_2 , and CO_2) [69, 70]. This method can either deliver a fixed concentration of CO_2 or target a subject-specific P_{ETCO_2} level for a period of time (~120 seconds) [23, 71-73]. Because this method allows subjects to inhale CO_2 passively, it is coined CO_2 inhalation or CI. Second, the breath-holding (BH) task requires subjects to hold their breath for short periods of time (~20 seconds). This method also results in an increase in P_{ETCO_2} and a subsequent increase in CBF [74, 75]. The BH task is a simpler means to induce hypercapnia compared to the CI task since it does not require additional specialized equipment.

Near-infrared spectroscopy (NIRS) is a non-invasive optical device that has been widely used to investigate concentrations of oxyhemoglobin ($\Delta[\text{HbO}]$) and deoxyhemoglobin ($\Delta[\text{Hb}]$) at the surface of the cortex, thereby providing measurements of cerebral blood flow (CBF), volume, and oxygenation changes [76-79]. Compared to functional magnetic resonance imaging (fMRI), NIRS is a low-cost, portable technology for studying brain function and physiology [78]. There are several benefits of using NIRS. For example, NIRS can provide real-time measurements (e.g.

football field) and bedside measurements (immobile people), as chronic brain damage has prompted concern for contact sport athletes [80-84].

Recently, some studies have used NIRS to study hypercapnia under the CI and BH tasks [85-91]. However, results from CI tasks have been inconsistent; this may be due to physiological noise coming from the skin and skull [92-94]. For example, two studies reported that NIRS signals correlated well with $P_{ET}CO_2$ under the CI task [85, 90], but other studies found that NIRS signals were not sensitive to $P_{ET}CO_2$ under the CI task [87-89]. The goals of this study were to better understand NIRS signals during different hypercapnia tasks and develop a robust and independent NIRS protocol to assess brain reaction to vasostimulus. The NIRS signals ($\Delta[HbO]$ and $\Delta[Hb]$) and fMRI blood oxygenation level-dependent (BOLD) signals were compared for consistency with the goal of validating NIRS as a portable fMRI proxy.

3.2 Materials and Methods

3.2.1 Protocol

This study was approved by Purdue University Institutional Review Board. Informed consent was obtained from all subjects. Ten healthy subjects (4 female, 6 male, age range 19-33, mean age 23 years) were recruited for several hypercapnia tasks measured by NIRS and fMRI concurrently (Figure 3-1 (a-f)).

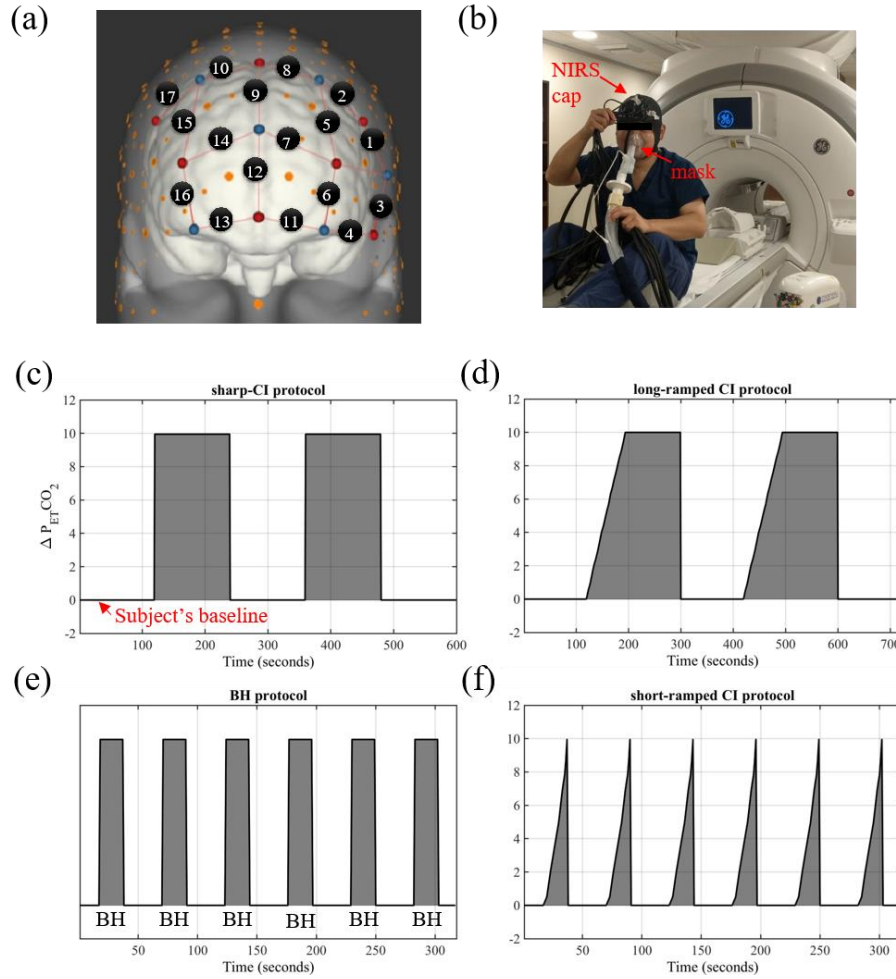


Figure 3-1 Experimental design and setup. Schematic of (a) Configuration of the NIRS channels on the head. (b) Experimental setup of the concurrent fMRI/NIRS experiments (c) the sharp-CI, (d) the long-ramped CI, (e) the BH, and (f) the short-ramped CI tasks [61].

3.2.2 Near-infrared Spectroscopy

The CW NIRS system (NIRScoutXP NIRx Medizintechnik GmbH; Berlin, Germany) and MRI-compatible NIRS probes with 10 m long optical fibers were used to measure $\Delta[HbO]$ and $\Delta[Hb]$. This system uses laser sources, each combining two wavelengths (785 nm and 830 nm). The source-detector distance was 3 cm. Vascular reactions to hypercapnia were recorded from the prefrontal region of the brain. Due to the limited space in MRI head coil, 17 NIRS channels (7 sources and 7 detectors) were deployed with a sampling rate of 7.8125 Hz (Figure. 3-1 (a)).

3.2.3 MRI

Functional MRI data were obtained using a 3T GE Discovery MR750 MR scanner (GE Electric; Milwaukee, WI, USA) and a 32-channel receiver head coil (Nova Medical, Inc.; Wilmington, MA, USA). The MRI scans were acquired using a multiband echo-planar imaging sequence (FOV = 216 mm, acquisition matrix = 72×72 , 60 slices, voxel size = $3 \times 3 \times 3$ mm³, TR/TE = 1000/30 ms, flip angle = 50°, hyperband acceleration factor = 4, phase acceleration factor = 1).

3.2.4 Sharp-CO₂ inhalation (Sharp-CI) task

For the sharp-CI task, varying CO₂ concentrations were supplied to each subject, through a sealed mask, by a computerized gas delivery system (RespirAct™, Thornhill Research Inc. Toronto, Canada) (Figure 3-1 (b)) [69]. P_{ET}CO₂ and P_{ET}O₂ were controlled and measured throughout the experiment. All subjects took part in pre-testing outside the MRI to ensure they were capable and comfortable performing the sharp-CI task. The pre-testing consisted of 1) a measurement of each subject's baseline P_{ET}CO₂, and 2) a short version of the sharp-CI task. The full task consisted of five two-minute blocks (Figure 3-1 (c)). The 1st, 3rd and 5th blocks were rest blocks where subjects inhaled normal air. The 2nd and 4th blocks were hypercapnia blocks where subjects inhaled air with sharply elevated CO₂ concentration that led to an increase of 10 mmHg above each subject's P_{ET}CO₂ baseline within one or two breaths. The P_{ET}CO₂ was then maintained at a high level for 2 minutes (Figure 3-1 (c)) [95].

3.2.5 Other induced-hypercapnia tasks

To further explain inconsistencies between the NIRS and fMRI signals under the sharp-CI task (Figs. 2 and 3), we conducted three additional concurrent-fMRI/NIRS experiments on 4 out of the original 10 subjects (2 male, 2 female, age range 20-29, mean age 22 years, subgroup). These additional experiments (i.e., long-ramped CI, BH, and short-ramped CI tasks) examined the effects of the rate of hypercapnia inducement on NIRS and fMRI data.

First, the sharp-CI task was modified to incorporate the long-ramped increase in P_{ET}CO₂, called the long-ramped CI task (as shown in figure 3-1 (d)) [90]. In short, during the hypercapnia

blocks, the $P_{ET}CO_2$ was slowly ramped up to 10 mmHg above the subject's baseline within 75 seconds and then maintained at that level for 105 seconds.

Second, the BH task was adopted from a widely used paradigm [96]. It consisted of 6 BH epochs (Figure 3-1 (e)); each epoch had 18 seconds of paced breathing (3 repetitions of a 3 second inhale followed by a 3 second exhale), followed by 20 seconds of BH, and then 15 seconds of normal breathing (total time = 5 minutes 18 seconds). To acquire consistent results from the BH task across all subjects, a gentle exhale was required before the BH [96]. An open-source package from PsychoPy was compiled to provide instructions to subjects and control procedures (i.e. paced breathing, BH, and normal breathing) [97].

Lastly, a short-ramped $P_{ET}CO_2$ was designed (Figure 3-1 (f)) to simulate the BH task via $P_{ET}CO_2$ control. In short, the short-ramped CI paradigm began with 18 seconds of rest followed by six blocks of alternating hypercapnia sections. The first hypercapnia section slowly ramped the subject's $P_{ET}CO_2$ to 10 mmHg above their baseline within 20 seconds, and the second section consisted of normal breathing for 33 seconds. The 10 mmHg increase of $P_{ET}CO_2$ was selected based on a study by Tancredi et al. (2013) which demonstrated that the $P_{ET}CO_2$ elevation after a 20 second BH was close to 10 mmHg [98].

3.2.6 Data analysis

All NIRS data were processed using the nirsLAB analysis package (v2016.05, NIRx Medical Technologies, LLC.; Los Angeles, USA) [99] and MATLAB (MATLAB 2018b, The MathWorks Inc., Natick, MA, 2000). NIRS signals with bad signal quality were eliminated (i.e. signals with no visible heartbeat signal). For the BH and short-ramped CI task, NIRS signals from those six cycles were parsed and aligned to calculate the folding-average result [32].

All MR data were processed using FSL (FMRIB Expert Analysis Tool, v6.01; Oxford University, UK [45]) and MATLAB. The fMRI BOLD signals acquired during the CI and BH tasks were preprocessed with the following steps recommended by Power et al. (2014): 1) motion correction (FSL mcflirt) and 2) spatial smoothing with a full width at half maximum (FWHM) of 5 mm isotropic Gaussian kernel [14]. For comparison with NIRS data, the percent change of averaged BOLD signal ($\Delta \overline{BOLD}\%$) from the prefrontal region was calculated to represent the intracerebral signal in the brain. In short, a prefrontal ROI was created on the standard structural brain and then warped onto each subject's fMRI space to extract the corresponding temporal fMRI

signals [100]. Lastly, the time series of BOLD signals from all the voxels were averaged (FSL `fslmeants`).

For the sharp-CI and long-ramped CI task, a zero-delay lowpass filter (0.1 Hz, 3th order) was used to extract the low-frequency signals ($\Delta P_{ET}CO_2$, $\Delta \overline{BOLD}\%$, $\Delta[HbO]$, and $\Delta[Hb]$), since both tasks contain low-frequency components (< 0.005 Hz). For BH, and short-ramped CI tasks, a zero-delay bandpass filter (0.01-0.1 Hz, 3th order) was used to extract the low-frequency signals.

To visualize the group result from each experiment averaged signals (signals obtained from fMRI/NIRS) from each subject were first normalized (subtracted by mean and divided by standard deviation) and then averaged by the number of subjects in the group.

To calculate the correlation between signals (NIRS signals, $\Delta \overline{BOLD}\%$, and $\Delta P_{ET}CO_2$), cross-correlation (MATLAB `xcorr`, lag range = ± 45 seconds) was performed, knowing time delays might exist among these signals. For statistical analysis, the maximum cross-correlation coefficients (MCCCs) were converted into Z-values using Fisher's Z-transformation [101, 102]. Then, a one-sample t test against zero was applied on the correlation Z-values. The significance level was set at $p < 0.05$, which was corrected for multiple comparisons using the false discovery rate (FDR) criterion [103]. For the additional induced-hypercapnia tasks (4 subjects), the p -value was not corrected for multiple comparisons due to the small sample size.

Movies were created to reflect the spatio-temporal changes of NIRS signals, $\Delta P_{ET}CO_2$, and especially the regional $\Delta \overline{BOLD}\%$ under hypercapnia tasks. Tasks included the sharp-CI task (one example with high correlations between $\Delta \overline{BOLD}\%$, $\Delta P_{ET}CO_2$, and NIRS signals and another example with low correlations), the breath-holding task, and the long-ramped CI task.

3.3 Materials and Methods

3.3.1 Sharp-CI results

Consistent $\Delta \overline{BOLD}\%$ were found across all subjects under the sharp-CI task, which were highly correlated to the waveform of $\Delta P_{ET}CO_2$ ($r = 0.89 \pm 0.07$, $p < 10^{-7}$). However, inconsistent NIRS signals were found across subjects. For example, averaged NIRS signals had much lower correlation values, and larger standard deviations, when $\Delta P_{ET}CO_2$ was increased sharply ($\Delta[HbO]$: $r = 0.45 \pm 0.44$, $p < 10^{-3}$; $\Delta[Hb]$: $r = -0.69 \pm 0.20$, $p < 10^{-4}$).

More importantly, averaged NIRS signals showed low correlation with $\Delta\overline{BOLD}\%$ ($\Delta[\text{HbO}]$: $r = 0.43 \pm 0.28$, $p < 10^{-3}$; $\Delta[\text{Hb}]$: $r = -0.51 \pm 0.32$, $p < 10^{-3}$). In fact, correlations between $\Delta\overline{BOLD}\%$ and NIRS signals were low in most of the channels (Figure 3-2) and the lowest averaged MCCC between $\Delta\overline{BOLD}\%$ and $\Delta[\text{HbO}]$ was 0.14. Also, the averaged MCCCs were spatially different. To highlight NIRS signal inconsistencies, two subjects are discussed in detail.

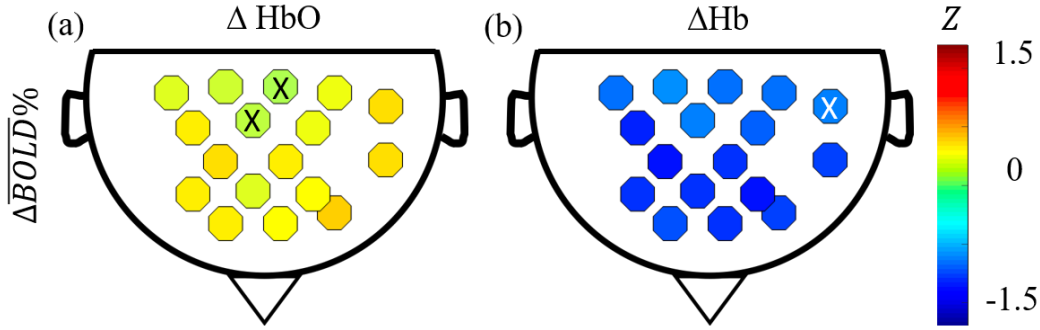


Figure 3-2 Averaged MCCC from each channel under the sharp-CI task. Averaged MCCC from each channel under the sharp-CI task between $\Delta\overline{BOLD}\%$ and (a) $\Delta[\text{HbO}]$, (b) $\Delta[\text{Hb}]$. Crosses in the channel indicate a p -value larger than 0.05 under the FDR-criterion [61].

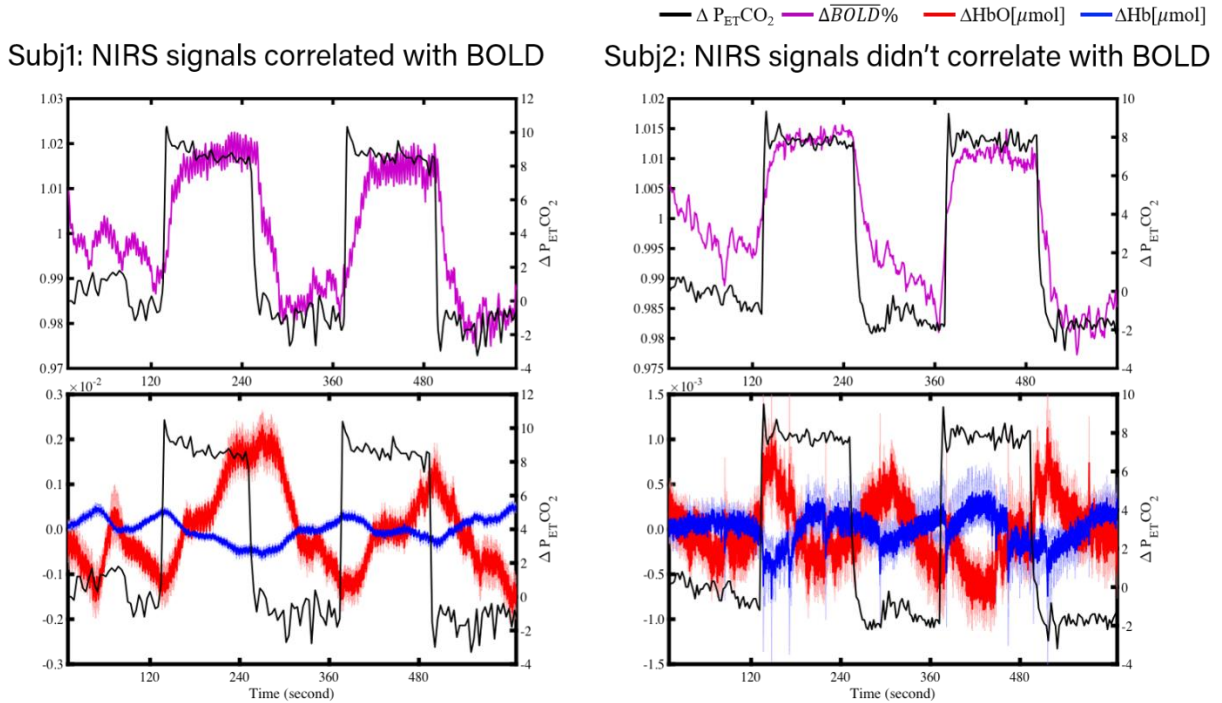


Figure 3-3 inconsistent NIRS signal during the sharp-CI task. Results showing inconsistencies in NIRS signals during the sharp-CI task from two example subjects in (a) and (b). The signals of $\Delta P_{\text{ET}}\text{CO}_2$, $\Delta\overline{BOLD}\%$, $\Delta[\text{HbO}]$, and $\Delta[\text{Hb}]$ are shown in the colors of black, purple, red, and blue respectively. The averaged results of $\Delta[\text{HbO}]$ and $\Delta[\text{Hb}]$ are shown at the bottom right of (a) and (b) in red boxes [61].

The results from the sharp-CI task observed from subject 1 presented good signal correlations between $\Delta\overline{BOLD}\%$, $\Delta P_{ET}CO_2$, and NIRS signals (Figure 3-3 (a)). Under the sharp-CI task, $\Delta\overline{BOLD}\%$ was highly correlated with $\Delta P_{ET}CO_2$ ($r = 0.86$) (Figure 3-3 (a)), indicating a fast-vascular reaction in the brain. Additionally, although MCCCs between NIRS signals and $\Delta\overline{BOLD}\%$ were not low ($\Delta[HbO]$: $r = 0.63 \pm 0.12$, $p < 10^{-9}$; $\Delta[Hb]$: $r = -0.57 \pm 0.13$, $p < 10^{-9}$), most $\Delta[HbO]/\Delta[Hb]$ signals responded slowly to the sharp increase of $\Delta P_{ET}CO_2$. Moreover, $\Delta[HbO]$ signals (e.g., CH16) continued to increase the following cessation of the hypercapnic block and it took a full two minutes to decrease during the resting block.

In another subject (e.g., subject 2), NIRS signals did not correlate well with $\Delta\overline{BOLD}\%$ (Figure 3-3 (b), $\Delta[HbO]$: $r = 0.08 \pm 0.20$, $p > 0.05$; $\Delta[Hb]$: $Z = -0.08 \pm 0.17$, $p > 0.05$), and didn't appear to react to the sharp-increase in $\Delta P_{ET}CO_2$. Further, the $\Delta[HbO]$ signals, which showed good signal quality and consistency among channels, hardly changed during the first hypercapnic block but instead increased during the resting block. Interestingly, $\Delta\overline{BOLD}\%$ for this subject increased sharply with a sharp increase in $\Delta P_{ET}CO_2$ ($Z = 0.94$), as seen with subject 1 (Figure 3-3 (a)).

3.3.2 Additional induced-hypercapnia tasks

The $\Delta P_{ET}CO_2$, $\Delta\overline{BOLD}\%$ and NIRS signals under the BH task, long-ramped CI, short-ramped CI, and sharp-CI task from 4 selected subjects were also averaged (Figure 3-4). In all tasks, $\Delta\overline{BOLD}\%$ signals were highly correlated with $\Delta P_{ET}CO_2$ ($r > 0.78$, $p < 0.05$), indicating robust and fast cerebral reactivity. However, there were profound differences in NIRS signals:

1. Sharp-CI task results from these 4 subjects were also included for ease of comparison.

Under the sharp-CI task (Figure 3-4 (a)), the MCCCs between NIRS signals and $\Delta\overline{BOLD}\%$ was relatively low ($\Delta[HbO]$: $r=0.47 \pm 0.55$, $p < 0.05$; $\Delta[Hb]$: $r = -0.32 \pm 0.45$, $p > 0.1$) with large standard deviations and long delays. These results are in line with the rest of the subjects discussed in section 3.3.1.

2. Under the BH task (Figure 3-4 (b)), both $\Delta[HbO]$ and $\Delta[Hb]$ signals were highly correlated with $\Delta\overline{BOLD}\%$ ($\Delta[HbO]$: $r = 0.77 \pm 0.1$, $p < 0.005$; $\Delta[Hb]$: $r = -0.58 \pm 0.11$, $p < 0.005$).

3. Under the long-ramped CI task (Figure 3-4 (c)), both $\Delta[\text{HbO}]$ and $\Delta[\text{Hb}]$ signals were highly correlated with $\Delta\overline{BOLD}\%$ ($\Delta[\text{HbO}]$: $r = 0.68 \pm 0.06$, $p < 10^{-3}$; $\Delta[\text{Hb}]$: $r = -0.62 \pm 0.15$, $p < 0.005$).
4. Under the short-ramped CI task (Figure 3-4 (d)), relatively low MCCCs were found between NIRS signals and $\Delta\overline{BOLD}\%$ ($\Delta[\text{HbO}]$: $r = 0.49 \pm 0.29$, $p < 0.05$; $\Delta[\text{Hb}]$: $r = -0.50 \pm 0.34$, $p < 0.05$). Furthermore, the standard deviations across NIRS results were large.

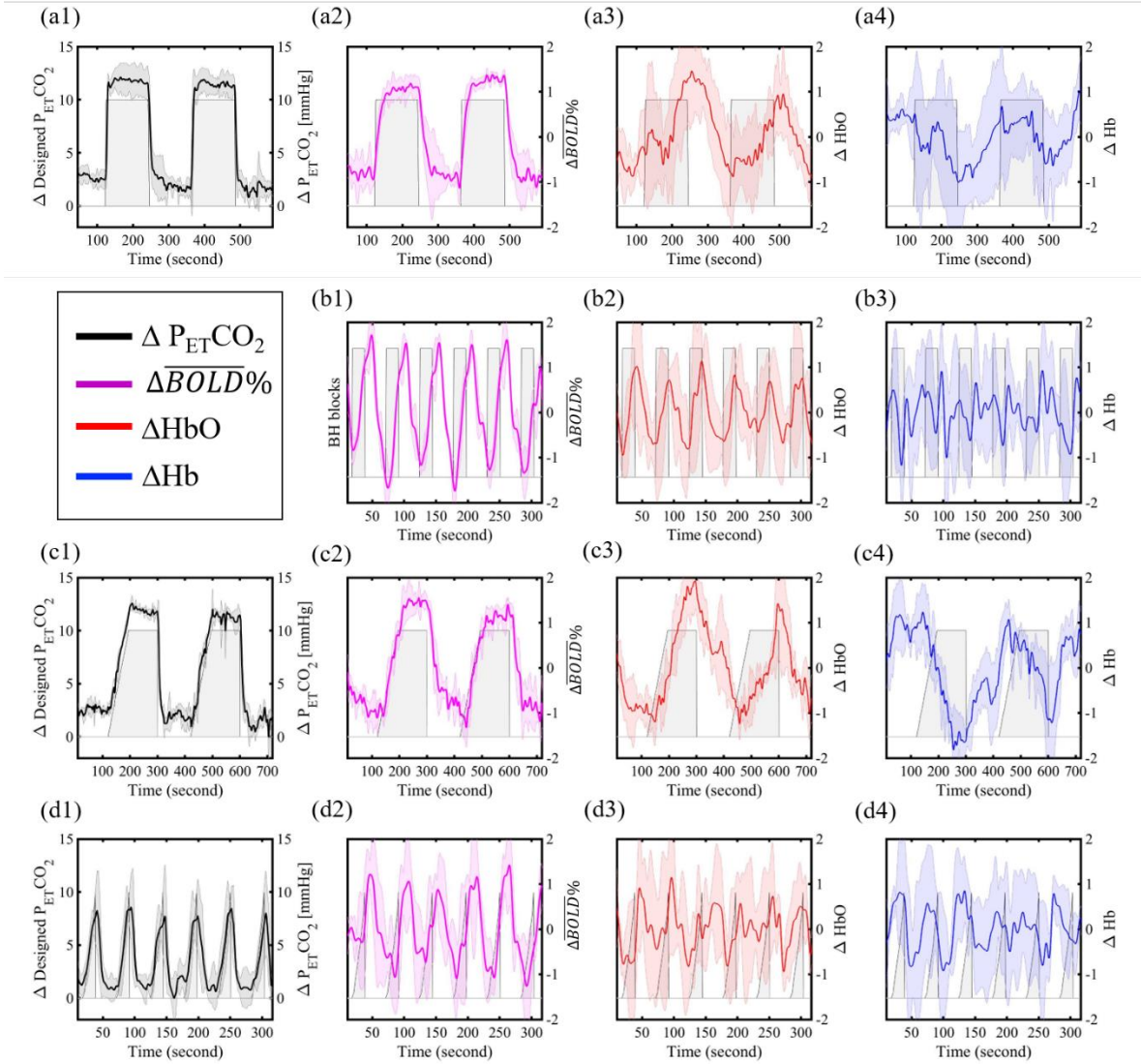


Figure 3-4 The fMRI and NIRS results from different hypercapnia tasks. The fMRI and NIRS results from the (a) sharp-CI tasks, (b) BH, (c) long-ramped CI, and (d) short-ramped CI. The shaded areas indicate the targeted $\Delta P_{ET}CO_2$ in each task. The averaged $\Delta P_{ET}CO_2$, $\Delta\overline{BOLD}\%$ (normalized), $\Delta[\text{HbO}]$, and $\Delta[\text{Hb}]$ signals are shown in columns 1-4, respectively [61].

The averaged MCCC between $\Delta\overline{BOLD}\%$ and NIRS signals of each channel and all tasks for the subgroup of 4 subjects were calculated (Figure 3-5). $\Delta[HbO]$ and $\Delta[Hb]$ signals were significantly correlated with $\Delta\overline{BOLD}\%$ for most channels in the BH, long-ramped CI, and short-ramped CI task (Figure 3-5 (a-c)). In contrast, figure 3-5 (d) shows that under the sharp-CI task, 47% of the $\Delta[HbO]$ signals and 82% of the $\Delta[Hb]$ signals were not significantly correlated with $\Delta\overline{BOLD}\%$.

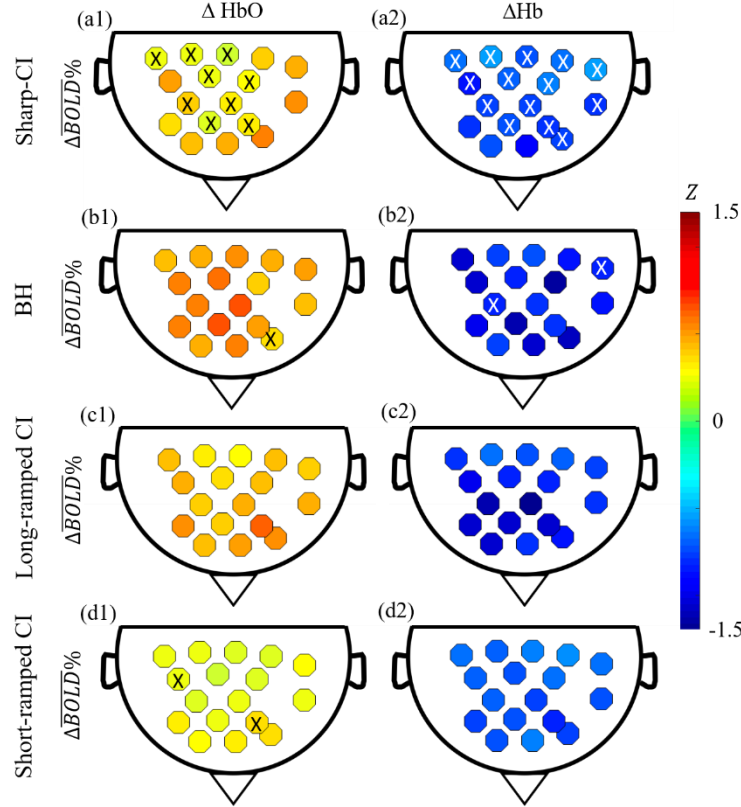


Figure 3-5 Averaged MCCCs between fMRI and NIRS signals. Averaged MCCCs between $\Delta\overline{BOLD}\%$ and $\Delta[HbO]$ ($\Delta[Hb]$) signals are shown in column 1 (2). The corresponding tasks are sharp-CI (a), BH (b), long-ramped CI (c), short-ramped CI (d). Crosses in the channel indicate a p -value larger than 0.05 under one-sample t -test [61].

Figure 3-6 illustrates three snapshots from one subject's long-ramped CI task movie. By mapping the spatio-temporal patterns of $\Delta\overline{BOLD}\%$ in the brain under hypercapnia tasks, we found that brain reactions to CO_2 are highly spatial-specific. As result, NIRS signals under hypercapnia are likely to be spatial-specific as well. Moreover, it was found that the $\Delta\overline{BOLD}\%$ signal from the superficial layer of the prefrontal region (black squares in Figure 3-6) reacted slower to CO_2 when compared to the deeper layer. This observation indicated that it was incorrect to claim that NIRS

signals reflect brain responses from all layers of the prefrontal cortex. Even without physiological noise from the skin and skull, NIRS may only measure responses in the superficial layer of the brain, which, based on our results, lagged the response from the deeper layer.

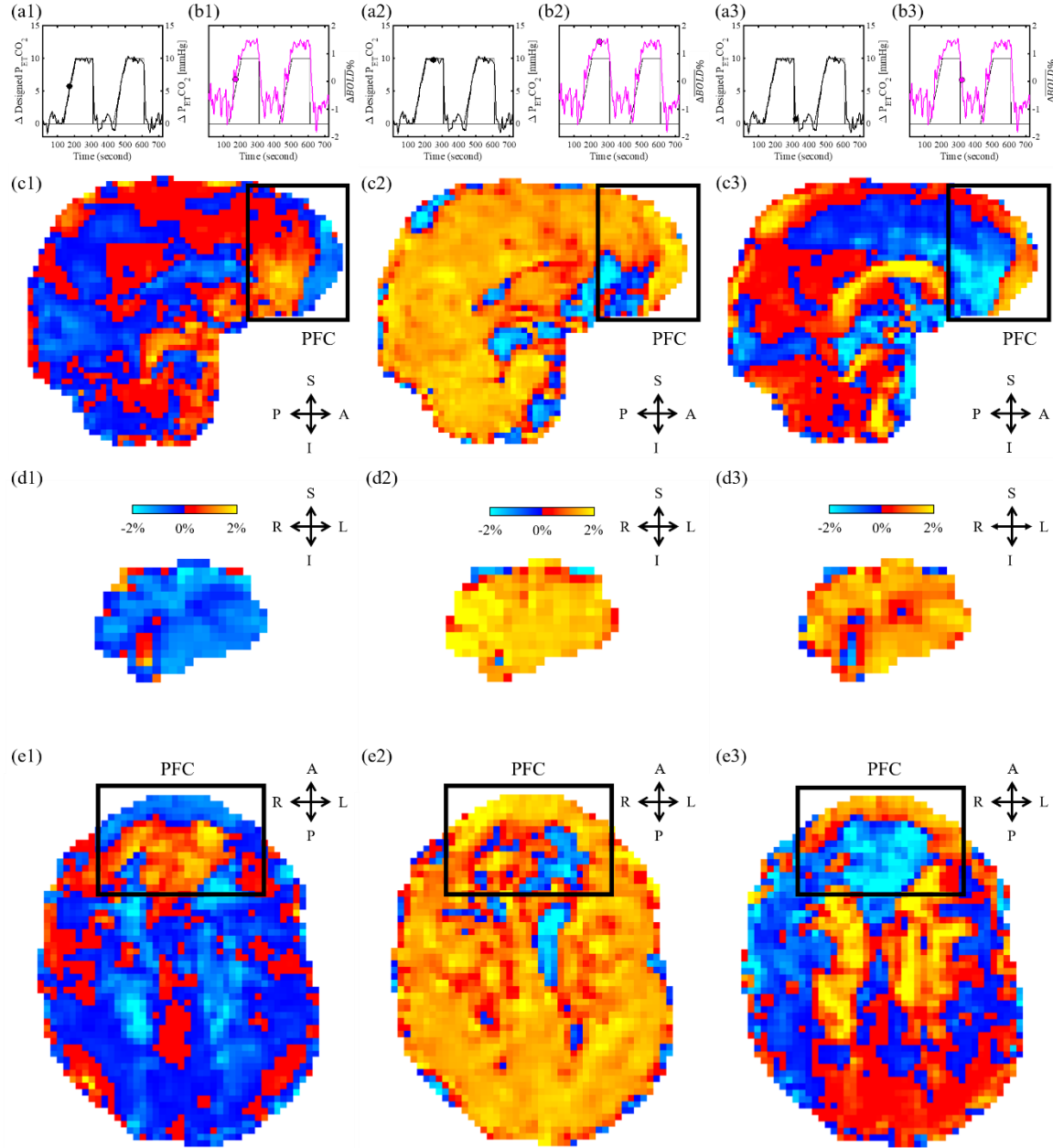


Figure 3-6 The fMRI movie snapshots from one subject under the long-ramped CI task. Three snapshots were captured at (1) rising phase (2) plateau, and (3) falling phase of $\Delta P_{ET}CO_2$ in the long-ramped CI task. During each time point, real-time (a) $\Delta P_{ET}CO_2$ and (b) $\Delta BOLD\%$ (normalized) signals are displayed. Also, $\Delta BOLD\%$ (normalized) maps (red-yellow refers to positive percent changes and blue-light blue refers to negative percent changes) in (c) sagittal, (d) coronal, and (e) axial views are shown. The shaded areas indicate the targeted $\Delta P_{ET}CO_2$ during the task. The black square in every (c) and (e) panel indicate the region of the prefrontal cortex (PFC) [61].

3.4 Discussion

The goal of this study was to better understand NIRS signals under induced-hypercapnia and establish and optimize a corresponding protocol so NIRS can be used in lieu of fMRI as an alternative, portable, methodology to acquire critical brain perfusion parameters (e.g. CVR).

3.4.1 NIRS signals under sharp-CI task

In the sharp-CI task (i.e., sharp increases in $\Delta P_{ET}CO_2$), the $\Delta \overline{BOLD}\%$ s from all subjects were highly correlated with the waveform of $\Delta P_{ET}CO_2$. However, NIRS reactions to the sharp increases in $\Delta P_{ET}CO_2$ were unpredictable and highly heterogeneous both temporally and spatially. The difference between the $\Delta \overline{BOLD}\%$ and NIRS signals relate to the fact that NIRS signals are sensitive to blood flow and volume changes in both the extracerebral *and* cerebral layers, while $\Delta \overline{BOLD}\%$ reflects these changes in the cerebrum only [104, 105].

Another possible explanation for the difference between $\Delta \overline{BOLD}\%$ and NIRS signals may be related to layer-specific differences in vascular reactions following exposure to sharp increases in $P_{ET}CO_2$. In fact, cerebrovascular responses are controlled by an autoregulation system [106], while extracerebral reactions are not [107]. A previous study found that the velocity of blood flow increased more in the cerebral circulation (about 54% increase in the internal carotid artery) than in the extracerebral circulation (about 5% increase in the external carotid artery) under a CI task (6% CO_2) [108]. Similar results were also found in another study, in which greater blood flow was observed in the middle cerebral artery (cerebral) compared to the brachial artery (extracerebral) [109]. These findings suggest that the cerebral vascular reaction is more sensitive to $P_{ET}CO_2$ elevation than the extracerebral and peripheral vascular reactions. This makes sense, intuitively, given the criticality of brain homeostasis. In detail, blood flow would be dramatically prioritized to the brain when $P_{ET}CO_2$ increases sharply, leading to a quick reaction observed in cerebral blood flow (observed by BOLD fMRI). In contrast, blood flow to the extracerebral layer could be dramatically compromised, leading to long delays, gradual increases, or sometimes, unpredictable changes in the extracerebral circulation (observed by NIRS).

The degree of the effect is dependent upon each individual's physiology (e.g., sensitivity to elevated $P_{ET}CO_2$, speed of blood flow adjustment, etc.) which could explain the highly varied NIRS results between subjects during the sharp-CI task. Based on these arguments, it is

hypothesized that the cerebral and extracerebral vascular reactions could be more easily synchronized when the $P_{ET}CO_2$ increase is not sharp, but instead slow and gradual. This gradual increase in $P_{ET}CO_2$ would provide adequate time for the carotid artery to meet the increasing demands for both cerebral and extracerebral circulation, leading to consistent NIRS signals that would correlate better to fMRI signals.

3.4.2 Validations

To test the hypothesis, we conducted three additional induced-hypercapnia tasks. Under the long-ramped CI task, $\Delta\overline{BOLD}\%$ and NIRS signals correlated well and showed slow and gradual increases (decreased $\Delta[Hb]$ signals), as suggested (Figure 3-4 (b)). Furthermore, it is reasonable to assume that $P_{ET}CO_2$ increases gradually during the BH period due to continuous and stable physiological demand and lack of air exchange. The post-exhale BH protocol used in the study [96] would raise $P_{ET}CO_2$ almost immediately (compared to BH after inhalation), but slowly. If the $P_{ET}CO_2$ increased slowly during the BH protocol, based on our hypothesis, the cerebral and extracerebral circulations should react almost simultaneously. This is exactly what was observed (Figure 3-4 (a)). NIRS and $\Delta\overline{BOLD}\%$ signals correlated well and showed gradual increases during the BH. The results are consistent with those from previous fMRI studies [86, 91, 110].

Additionally, under the long-ramped CI, most of the NIRS signals had slower responses compared to the BOLD fMRI signal, which was also observed in a previous vasostimulus study (CI task) [90]. However, the observations were different from the concurrent studies on the functional/cognitive tasks (e.g. finger tapping task, go/no go task), which showed that the NIRS ($\Delta[HbO]$) reacted faster and had shorter time-to-peaks than BOLD fMRI signals [92, 111, 112]. The observed differences are caused by varying brain reactions to neuronal and physiological stimuli. First, the NIRS/fMRI signal from the cognitive task results from neurovascular coupling, which is regional, while the signal in vasostimulus task results from the vasodilatory effect of CO_2 , which is global (including skin and skull). Secondly, cognitive activation is instantaneous, while elevated CO_2 must be carried by the blood and may reach different brain regions with varying time delays. Thirdly, different brain regions react differently to arriving CO_2 based on the local hemodynamic response function, which can lead to further delays. In figure 3-6, we observed that the $\Delta\overline{BOLD}\%$ response to CO_2 was significantly lagged at the superficial layer of the prefrontal cortex when compared to deeper cortical layers. Since the NIRS probe was placed over the

prefrontal area, the lagged signal could be captured by the NIRS probe, thus resulting in observed delays.

Lastly, the short-ramped CI task was introduced to simulate the BH task (validating the gradual increase of $P_{ET}CO_2$ during the BH). The NIRS signal ($\Delta[HbO]$, (Figure 3-4 (c)) was expected to be similar to the signal obtained from the BH task (Figure 3-4 (a)). The results demonstrated that the NIRS signal does change according to the task (Figure 3-4 (c)), albeit with much more noise than that of BH task-related signals (Figure 3-4 (a)). The main reason could be that subjects had to physically breathe in order to reach the $P_{ET}CO_2$ level during the short-ramped CI task, while during the BH, no breathing was required. As result, NIRS signals in the short-ramped CI task may have been influenced by the side effects of respiration, such as motion and other related physiological processes. To remove the noise, a folding average of the NIRS signals (Figure 3-7) was calculated. The averaged NIRS epoch signals from the short-ramped CI task (Figure 3-7 (a)) and BH (Figure 3-7 (b)) were similar, and both were highly correlated with averaged $\Delta\overline{BOLD}\%$ signals. The delay observed in the data from the short-ramped CI task may have been due to the time lag for the inhaled CO_2 to reach the brain.

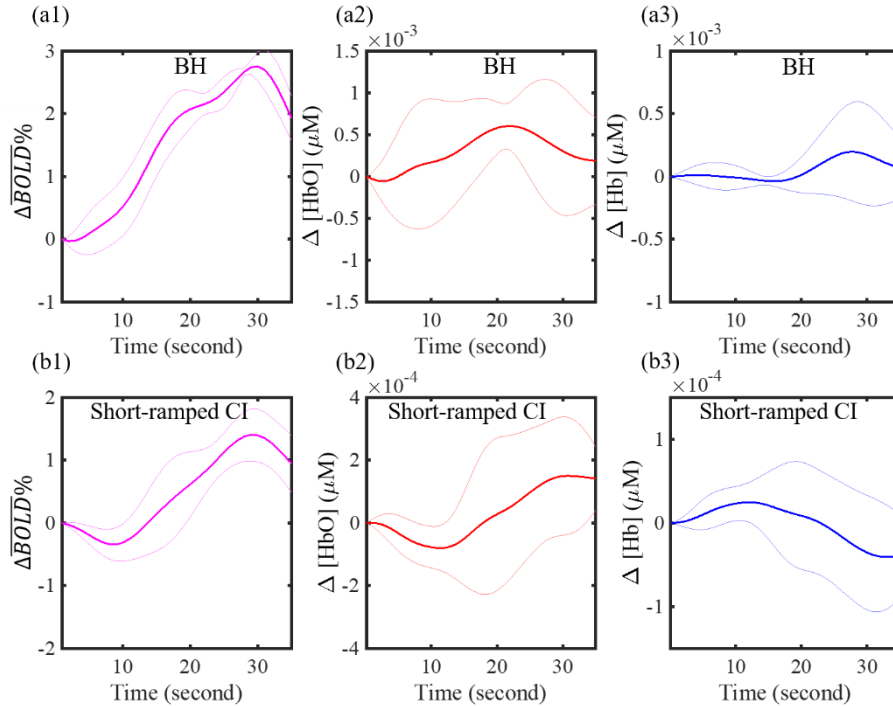


Figure 3-7 Group folding average of signals from the (a) BH and (b) short-ramped CI task. The results of $\Delta\overline{BOLD}\%$ (normalized), $\Delta[HbO]$, and $\Delta[Hb]$ are showed in columns 1-3, respectively. The time ranged from 0 to 20 second indicates the periods of BH/ramped-increased $\Delta P_{ET}CO_2$ [61].

3.4.3 Limitations

This study provides possible physiological explanations for the discrepancies observed between BH- and CI-related NIRS signals; however, several limitations exist. First, the source-detector distance was about 3 cm, which is commonly used in NIRS studies [88, 89]. However, other studies used longer source-detector distances (≥ 4 cm) and were, therefore, less prone to signals from the extracerebral layers and; consequently, these studies demonstrated more robust and consistent NIRS results [85, 88, 90]. Secondly, during the BH period, it was difficult to assess $P_{ET}CO_2$ changes (i.e. there was no exhaled breath to measure). Third, the NIRS probe was placed over the prefrontal region, which is a popular region of interest since there is little-to-no hair. However, this study found that hemodynamic responses under hypercapnia tasks are highly spatial-specific. Thus, whole-brain measurements using NIRS channels may be required to capture region-specific reactions to hypercapnia tasks. Lastly, future studies should incorporate measuring $P_{ET}CO_2$ changes that occur during the BH task. For example, previous studies required subjects to perform a forced exhalation at the end of each BH period – this could be incorporated in future studies [98, 110].

3.5 Conclusion

In summary, the presented study, together with previous studies, support the hypothesis that cerebral and extracerebral reactivity to elevated $P_{ET}CO_2$ is similar when the increase of $P_{ET}CO_2$ is gradual and is different when the increase of $P_{ET}CO_2$ is sharp. Further, it demonstrated that NIRS can be deployed as an alternative low-cost, real-time, and non-invasive methodology for reliably measuring the cerebrovascular reaction given the correct vasoactive stress tests (e.g. long-ramped CI and BH task). This would benefit a large population who require timely (e.g. athletes) and/or on-site (e.g. infants or patients with immobility) measurements of cerebral reactivity.

4. STUDY 3

4.1 Introduction

The glymphatic system plays an important role in the clearance of metabolic waste products in the extracellular interstitial space [113, 114] and the distribution of homeostasis-sustaining compounds (e.g., glucose) in the brain [115]. Recent advancements of the glymphatic system highlight its role in the development of neurodegenerative diseases. Unlike blood flow, which is driven by the heart pumping, CSF does not appear to have an engine to generate flow. Thus, CSF flow has been assumed to be mostly facilitated by the mechanisms associated with vessel wall movement (blood flow), including vasomotion [116, 117], pulsation [118], and/or inspiratory thoracic pressure changes [119, 120].

Several magnetic resonance imaging (MRI) techniques have been used to investigate CSF flow in the brain, including 1) phase-contrast imaging [121]; 2) velocity density imaging [122]; 3) time-spatial labeling inversion pulse imaging [123]; and 4) 4D flow MRI [124]. These imaging techniques were often used to detect the direction of CSF motion within a single cardiac/respiration cycle. However, they cannot reveal real-time CSF flow over a longer period or bulk flow.

Recently, Fultz et al used fast Echo-planar imaging (EPI) sequence ($TR < 400\text{ms}$) to study bulk CSF flow [125]. They ingeniously placed the edge of the imaging volume (the first slice) at the fourth ventricle, which allows them to measure the flow of CSF using the inflow effect [126] in the fMRI signal (rather than blood-oxygen-level-dependent (BOLD) contrast). They discovered a coherent pattern of oscillating electrophysiological, hemodynamic, and CSF dynamics that appears during non-rapid eye movement (NREM) sleep. Their results suggested the coupling between CSF inflow and the hemodynamic signal is related to waste clearance from the brain during sleep. While still a qualitative approach to the measurement of CSF flux, the advantages of the fast EPI approach are obvious. First, the fast EPI sequence is widely available, and the data processing is straightforward. Second, through simultaneous recording, coupling between brain hemodynamics and CSF flow, which is crucial in understanding the fundamental driving mechanism of CSF flow, can be examined. In this case, hemodynamics and CSF flow can be assessed by BOLD and in-flow contrast of fMRI respectively.

While effective and innovative, the study by Fultz et al. raises several scientific questions. First, they reported correlations between the derivative of the averaged fMRI signal in gray matter with CSF inflow signal; however, no detailed mechanistic explanation was given. Second, similar coupling was not fully explored during the awake state. Last, due to the limitation of the scan parameters, their method could only assess the inflow of CSF to the brain, but not the outflow from the fourth ventricle (i.e., to the neck). The difference between these two bulk flow rates would be indicative of the overall CSF flux.

This study was designed to address these questions. First, we proposed a simple mechanical model to explain the relationships between CSF movement and hemodynamic fluctuations in fMRI signal. Second, we investigated the coupling between brain hemodynamics and CSF flow during the awake state by an fMRI scan. Last, an additional fMRI scan was employed to assess CSF outflow and compare it with brain hemodynamics.

4.2 Materials and Methods

4.2.1 Model

The brain is in a rigid container. As a result, the volumes of the constituents (blood, CSF, and brain parenchyma) consistently fluctuate to maintain the total volume needed for proper internal pressure—i.e., the Monro-Kellie doctrine [127]. According to this doctrine, the transfer of movements from the arterial walls into the surrounding tissue will eventually cause CSF flow into and out of the spinal canal [128-130]. Multiple mechanisms cause arterial wall oscillations at various frequencies, such as cardiac pulsation ($\sim 1\text{Hz}$) and vasomotion ($<0.1\text{Hz}$). They have all been shown to produce the flow of CSF [116-120]. However, how to interpret the coupling between hemodynamic and CSF flow changes using fMRI signal is still not clear.

Here, we offer a general model that explains the coupling between these fMRI signals (hemodynamic and CSF flow changes). The model is based on the hypothesis that the accumulative effects of vessel dilations and contractions (pulsation, vasomotion) will exert force on the walls of ventricles, especially the lateral ventricles (no blood vessel in the ventricles), forcing CSF in and out of the fourth ventricle at the bottom (see figure 4-1). In this model, the global mean of fMRI signals (GMS) is used as a surrogate signal to indirectly assess the accumulative effects of vessel dilations and contractions in the brain [20, 26]. In figure 4-1, we

simulated volume changes in blood vessels and their consequential CSF flow observed at the fourth ventricle. In detail, the blood-rich region will expand because of vessel dilation. This will compress the volume of the lateral ventricle, forcing CSF out of the brain. The reverse happens when the vessels contract. However, the key point here is that CSF flow only happens at the transitions, during which the cerebral blood volume (CBV) changes (as shown by the arrows in figure 4-1). When CBV is stabilized, no force is exerted on the ventricular wall, thus no flow of CSF. Therefore, the model predicts CSF outflow at the fourth ventricle during CBV transition from low to high and CSF inflow during CBV transition from high to low. Since GMS of fMRI roughly represents CBV in the brain, the transitions are accurately captured by the derivative of GMS ($\frac{d}{dt}(\text{GMS})$), not GMS itself.

Based on this model, we have several predictions (Figure 4-1): 1) CSF inflow signal should be negatively correlated with $\frac{d}{dt}(\text{GMS})$; 2) since CBV change in the brain is the cause of CSF flow and the brain is not a rigid body, the CSF inflow signal should lag behind $\frac{d}{dt}(\text{GMS})$; 3) CSF outflow signal (towards the neck) should be positively correlated with $\frac{d}{dt}(\text{GMS})$ and lag behind $\frac{d}{dt}(\text{GMS})$ for the same reason as in (2). To assess these predictions, we have conducted the following studies using specially designed scan locations and sequences.

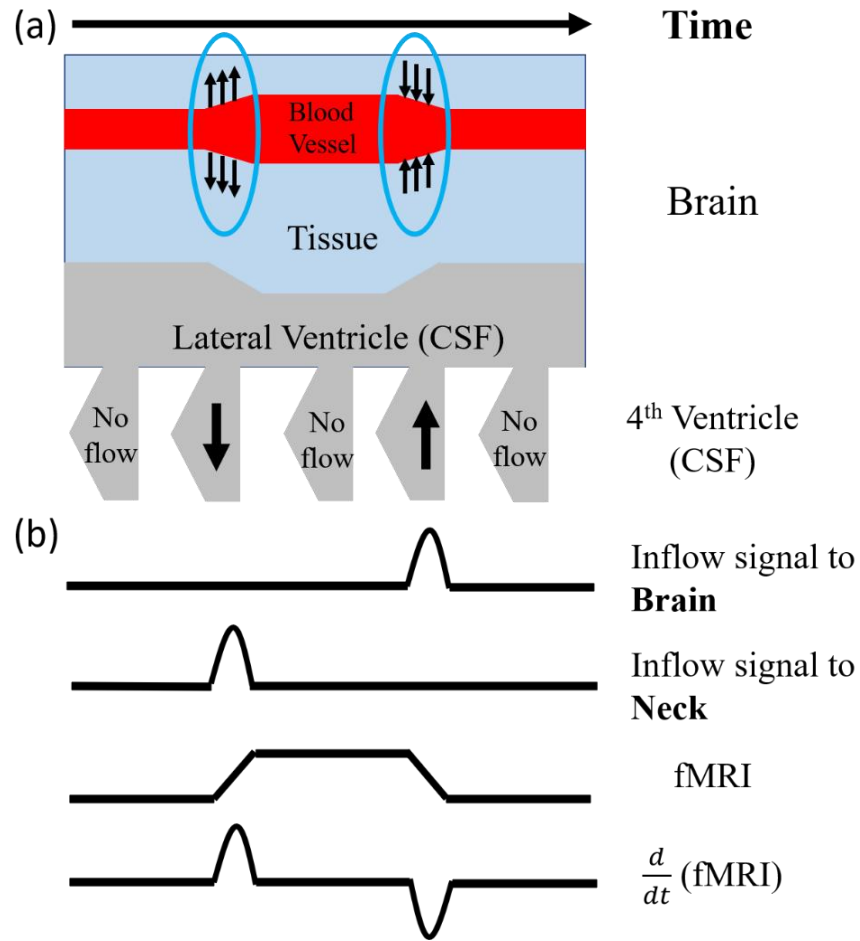


Figure 4-1 The brain model and its corresponding fMRI signals measured at the fourth ventricle and brain (GMS). (a) The model illustrates the temporal changes in vessel volume with the corresponding effects on the lateral ventricle shape and CSF flow at the fourth ventricle. Blue circles show periods of vessel volume change (i.e., transition). Arrows in the blue circles point to the direction of vessel wall movement. (b) Corresponding signals and their derivatives are observed at the fourth ventricle, brain (GMS). The flow signal is from the inflow ('time of flight') effect. The brain fMRI signal is from the BOLD effect.

4.2.2 Experimental Design

Structure Scans

This study was approved by the Purdue University Institutional Review Board. Informed consent was obtained from all participants. Ten healthy individuals (5 female, 5 male, age range 23-30 years) were recruited. MRI data were obtained using a 3T SIEMENS MRI scanner (Magnetom Prisma, Siemens Medical Solutions, Erlangen, Germany) and a 64-channel head coil. Each participant has one T1-weighted, one T2-weighted, and two functional scans. For T1-weighted scans, multiplanar rapidly acquired gradient-echo (MPRAGE) structural images were

acquired with the following parameters (TR/TE: 2300/2.26 ms, 192 slices per slab, flip angle: 8 deg, resolution: 1.0mm \times 1.0mm \times 1.0mm). Parameters for T2-weighted scans were as follows (TR/TE: 2800/409 ms, 208 slices per slab, resolution: 0.8mm \times 0.8mm \times 0.7mm). Since this study has two fast EPI MRI scans covering the head and neck respectively (Figure 4-2), long T1-w and T2-w images covering the head and neck were taken.

EPI Scans

The functional resting state (RS) scans were acquired using a multiband echo-planar imaging sequence (FOV = 230 mm, acquisition matrix = 92 \times 92, 48 slices, voxel size = 2.5 \times 2.5 \times 2.5 mm³, TR/TE = 440/30.6 ms, echo-spacing=0.51 ms, flip angle = 35°, hyperband acceleration factor = 8, multi-slice mode: interleaved). Participants were instructed to stay awake during the RS scans. CSF inflow captured by fast EPI sequence was discussed in detail in Fultz et al [125]. In short, as fresh fluid particles (not experienced radiofrequency pulses) move into the imaging volume, they induce higher signal intensity (i.e., inflow effect). To capture the inflow effect in both directions in the fourth ventricle, two 5-minute RS scans with different regions of interest were included. Both scans are positioned with the edge of the volume placed at bottom of the fourth ventricle (see figure 4-2 (a,b)), with one scan extending upward toward the top of the head (i.e., brain scan) and another scan extending downward into the neck (i.e., neck scan). As result, CSF inflow to the brain can be assessed by the brain scan, while CSF outflow from the brain can be assessed by the neck scan (i.e., considered as “inflow” to the scan volume that is the neck), under the assumption that flow sensitivity in the opposite directions can be ignored due to steady-state excitation in those slices either above or below the slice of interest. The slice of interest, at the fourth ventricle, was consistently acquired firstly in the TR.

4.2.3 Data analysis

CSF flow signals

All MR data were processed using FSL (FMRIB Expert Analysis Tool, v6.01; Oxford University, UK [45]) and MATLAB. For analysis of CSF flow dynamics, a voxel in the fourth ventricle in the edge slice of the EPI data was identified with help of the T1-weighted image

(registered onto the EPI data). The time series of the voxel was extracted to represent CSF flow. For CSF inflow, the signal was extracted from the bottom EPI slice of the head scan as shown in figure 4-2 (a, c). For CSF outflow, the signal was extracted from the top slice of the neck scan as shown in figure 4-2 (b, d). We hereafter refer to these two signals as “CSF inflow” and “CSF outflow”, even though they both stem from the inflow effect in fMRI.

Preprocessing

Since motion correction cannot be accurately performed on edge slices (given that tissue moves in and out of the imaging volume), only the slice-timing correction was performed prior to CSF flow signal extraction [125]. Then RS-fMRI data were preprocessed with the steps recommended by Power et al. [14]: 1) slice-timing correction (FSL *slicetimer*) 2) motion correction (FSL *mcflirt*) and 3) spatial smoothing with a full width at half maximum (FWHM) of 5 mm isotropic Gaussian kernel.

4.2.4 Data and statistical analysis

Segmentation was performed on the structural image. Several masks were made to investigate the coupling between CSF inflow signal and fMRI signal from these segmentations (Figure 2 (e)). First, anatomical masks for gray matter, white matter, and CSF were made using an automated segmentation program (FSL *fast*) [131]. Second, we identified large veins in the neck (i.e., internal jugular veins (IJVs)) and made corresponding masks (Figure 2 (f)). In a previous RS fMRI study, we found consistent positive correlations (>0.8) between GMS of the brain and the fMRI signal from the IJVs [132]. Therefore, here we used the fMRI signal from the IJVs as a surrogate signal of GMS (of the brain) in the neck scan. Detailed information about IJV mask identification can be found in a previous publication [132].

After extraction, the fMRI signals, including CSF flow signals (fourth ventricle), GMS from gray matter, white matter, and CSF, and signals from big veins (IJV), were first linearly detrended, and then band-pass filtered (0.01 to 0.1 Hz) using a zero delay, fourth-order Butterworth filter to extract the low-frequency oscillations (LFO). Cross correlations (MATLAB *xcorr*, lag range = ± 45 seconds) were calculated between (1) $\frac{d}{dt}$ (GMS) and CSF inflow signals, and (2) $\frac{d}{dt}$ (IJV) and CSF outflow signals. The maximal cross-correlation coefficients (MCCC) and the corresponding

delays were calculated for all the research participants. One-sample t-test against mean value was applied on MCCCs and corresponding delays calculated between (1) $\frac{d}{dt}$ (GMS) and CSF inflow signals, and (2) $\frac{d}{dt}$ (IJV) and CSF outflow signals for all the research participants. Moreover, to assess the coupling between CSF inflow signal with the whole brain and understand any spatial relationship, CSF inflow signal was cross-correlated with $\frac{d}{dt}$ (fMRI signal) for every voxel in the brain. The MCCC and delay maps were derived for each participant, and the average was also calculated.

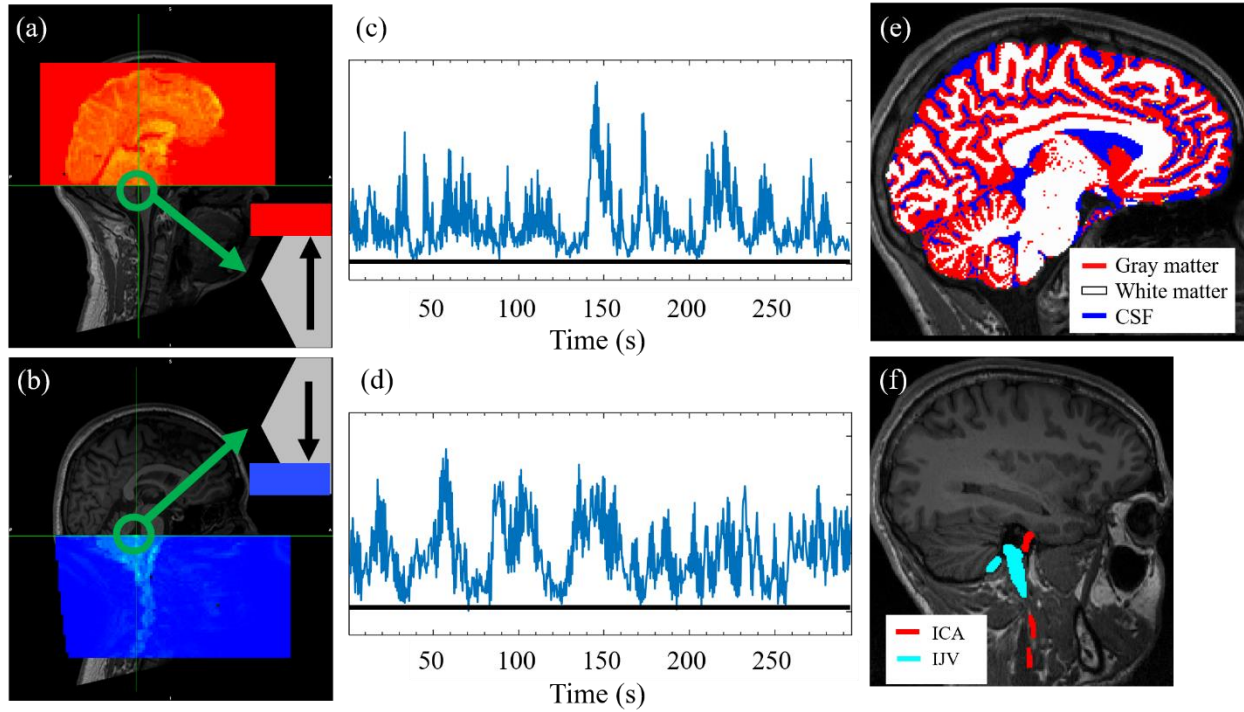


Figure 4-2 The scan designs and corresponding CSF flow signals. The scan volumes used in the brain scan (a) and the neck scan (b). In the brain scan (a), the signal detected at the first slice (green circle) represents CSF flow into the brain. In the neck scan (b), the signal detected at the first slice (green circle) represents CSF flow into the neck. The corresponding unfiltered, raw time series extracted from the green circles in (a) and (b), are shown in (c) and (d) respectively. They represent CSF flow signals to the brain (c) and to the neck (d). Both show large slow oscillations in addition to rapid oscillations due to cardiac pulsation. (e) Brain segmentation is used to identify gray matter, white matter, and CSF. (f) Blood vessel segmentation in the neck to identify internal jugular veins (IJV).

4.3 Results

4.3.1 CSF flow during wakefulness

Figure 4-2 (e) shows an example CSF flow signal obtained from the brain scan. First, it shows that during an awake state, CSF inflow signal is clearly detectable. Second, CSF outflow

(Figure 4-2 (f)) was clearly captured in the neck scan, as predicted by the model, indicating that the low-frequency CSF flow is also bi-directional. Note that CSF flow signals are unidirectional in each scan, leading to a flat baseline after detrending (black lines in figure 4-2 (e) and (f)). This is because the signal originates from the inflow effect which is sensitive to CSF flow in one direction only (i.e., into the scan volume). When CSF flows in the opposite direction, there is no inflow signal enhancement (i.e., flat). Furthermore, from figure 4-2 (e, f), the area under CSF signal fluctuation curves should reflect the amount of CSF flowing in each direction during the period of the scan.

4.3.2 CSF flow signal and $\frac{d}{dt}(\text{GMS})$

Figure 4-3 displays example low-frequency data from one research participant. It shows $\frac{d}{dt}(\text{GMS})$ of the brain and CSF inflow signal in (a-c), and the same participant's $\frac{d}{dt}(\text{IJV})$ and CSF outflow in (d-f). As mentioned, when describing the model, $\frac{d}{dt}(\text{GMS})$ is sensitive to the transitions of CBV in the brain, where a larger signal indicates a faster transition. During these transition times, CSF was forced to flow in and out of the brain (through the fourth ventricle). Specifically, positive signals in $\frac{d}{dt}(\text{GMS})$ related to CSF outflow, while negative signals in $\frac{d}{dt}(\text{GMS})$ related to CSF inflow. As shown in figure 4-3, CSF inflow signal matched the lower part of $\frac{d}{dt}(\text{GMS})$ in (b) (CSF inflow signal was flipped for demonstration; $\text{MCCC} = -0.75$), while CSF outflow signal matched the upper part of $\frac{d}{dt}(\text{IJV})$ in (e) ($\text{MCCC} = 0.83$). Note that, here we used $\frac{d}{dt}(\text{IJV})$ to represent $\frac{d}{dt}(\text{GMS})$. Thus, CSF outflow signal matched the upper part of $\frac{d}{dt}(\text{GMS})$. Moreover, this result also indicated that $\frac{d}{dt}(\text{GMS})$, unlike CSF flow signal that can only report the flow in one direction, is able to reflect CSF flow in both directions. Last, from the delays, CSF inflow lagged $\frac{d}{dt}(\text{GMS})$ by about 2.2s (Figure 4-3 (c)). This delay was predicted by the model, indicating CBV changes are likely the “cause” for CSF flow, though maybe not the only one. Similar results in delay were also shown in figure 4-3 (f). However, CSF outflow signal is leading $\frac{d}{dt}(\text{IJV})$ signal by about 2.2 s. From previous studies, the fMRI signal of IJV lags GMS by about 4 seconds [132].

After the adjustment for this delay, CSF outflow signal should still be lagging the true $\frac{d}{dt}$ (GMS)—i.e., the brain signal—by about 2 seconds, which is consistent with the findings in figure 4-3 (a-c).

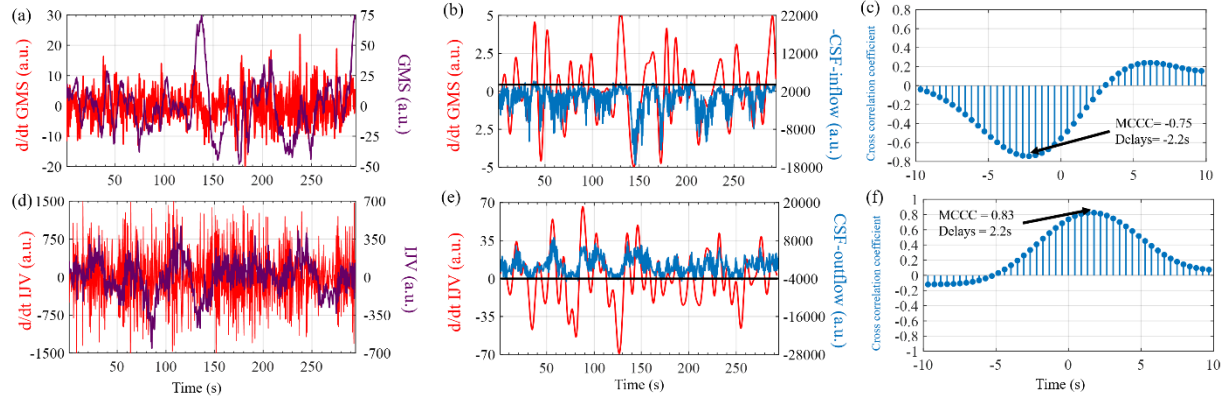


Figure 4-3 The relationships between GMS of the brain, CSF inflow signal (a-c), averaged IJV signal and CSF outflow signal (d-f) from the same research participant. (a) Time series of GMS in purple and its derivatives ($\frac{d}{dt}$ (GMS)) in red. (b) Time series of filtered $\frac{d}{dt}$ (GMS) in red with the negative raw CSF inflow signal in blue. It shows CSF inflow signal matches the lower part of filtered $\frac{d}{dt}$ (GMS). (c) Cross-correlation between filtered $\frac{d}{dt}$ (GMS) and CSF inflow signal shows the $\frac{d}{dt}$ (GMS) is ahead of CSF inflow signal with high MCCC (-0.75). (d) Time series of IJV signal in purple and the derivative of IJV ($\frac{d}{dt}$ (IJV)) in red. (e) The time series of filtered $\frac{d}{dt}$ (IJV) in red and CSF outflow signal in blue. It shows CSF outflow signal matches the top part of filtered $\frac{d}{dt}$ (IJV). (f) Cross-correlation between filtered $\frac{d}{dt}$ (IJV) and CSF outflow signal shows $\frac{d}{dt}$ (IJV) is a little behind of CSF outflow signal with high MCCC. GMS: global mean signal. MCCC: maximum cross-correlation coefficient. IJV: internal jugular vein task.

Figure 4-4 (a) shows the individual and average results of MCCC and delay calculated between $\frac{d}{dt}$ (GMS) and CSF inflow signal from the brain scans. Here $\frac{d}{dt}$ (GMS) was calculated from the gray matter, white matter, and CSF-region in the brain. The MCCC from all the participants are high for all the tissue types (MCCC for gray matter: -0.76 ± 0.07 ; for white matter: -0.69 ± 0.10 ; and for CSF: -0.76 ± 0.07 ($p < 10^{-8}$ for all)). The corresponding delays are around -2s—i.e., $\frac{d}{dt}$ (GMS) signal is leading CSF inflow signal. Among the three tissue types, $\frac{d}{dt}$ (GMS) from gray matter, white matter, and CSF-region led CSF inflow by 2.2 ± 0.55 s, 2.02 ± 0.69 s, and 1.36 ± 0.60 s ($p < 10^{-4}$ for all), respectively. Figure 4-4 (b) shows the average results of MCCC and delays calculated between $\frac{d}{dt}$ (IJV) and CSF outflow signal. The averaged MCCC is 0.64 ± 0.30 s ($p < 10^{-4}$) with an averaged delay of 0.66 ± 3.39 s ($p > 0.05$). As we mentioned previously, after adjustment for

the delay between fMRI signal of IJV and GMS (~ 4 s), CSF outflow signal should lag the brain signal ($\frac{d}{dt}(\text{GMS})$) by about 2s [18].

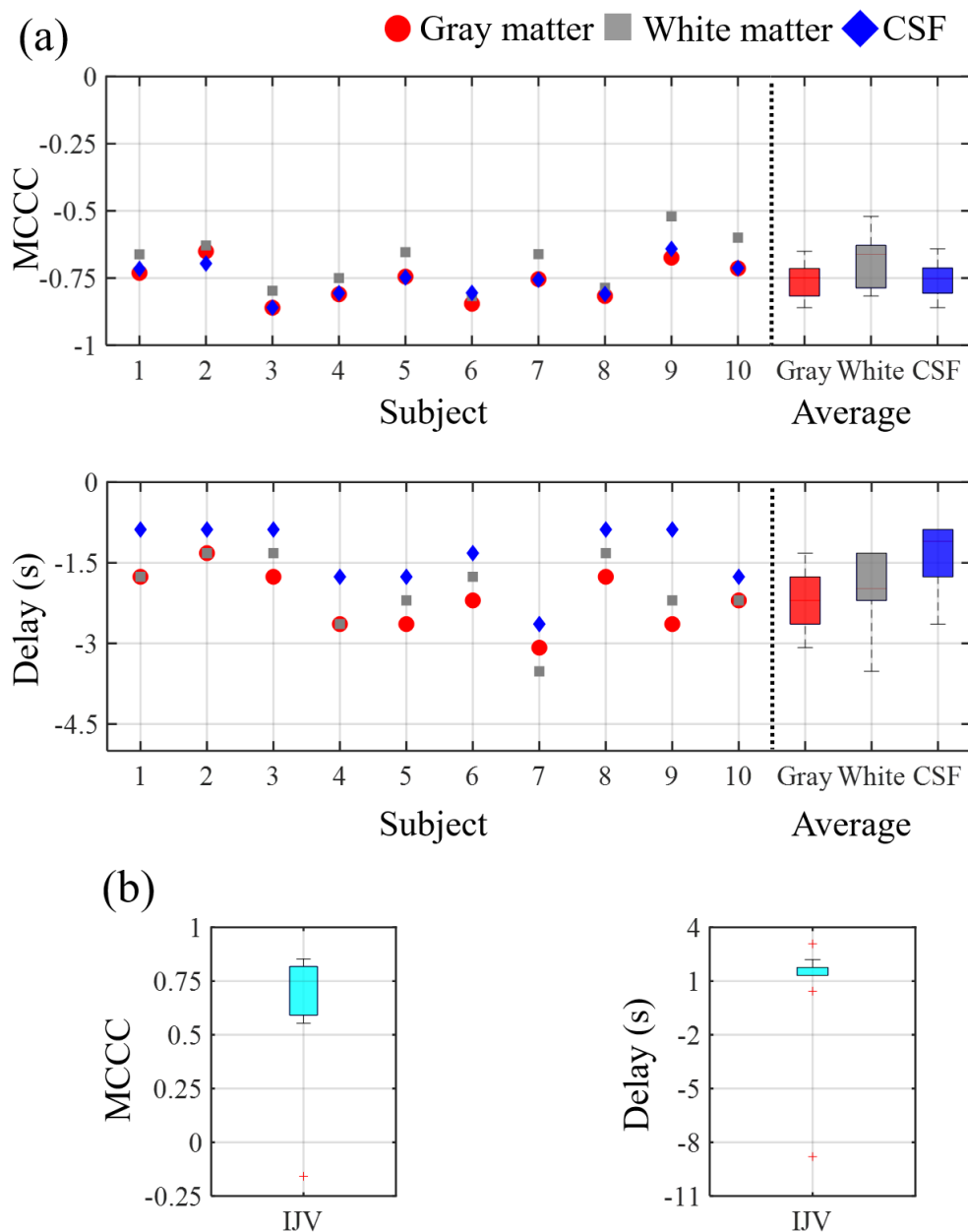


Figure 4-4 The summary of the cross-correlations between CSF inflow signal and $\frac{d}{dt}(\text{GMS})$ from different regions of interest (ROIs). (a) MCCCs and delays between CSF inflow signal and $\frac{d}{dt}(\text{gray matter})$, $\frac{d}{dt}(\text{white matter})$, $\frac{d}{dt}(\text{CSF})$ in each participant and the averaged result from all participants. All the $\frac{d}{dt}(\text{GMS})$ in different ROIs are temporally ahead of CSF inflow signal with high negative MCCCs. (b) Averaged MCCCs and delays between CSF outflow signal and $\frac{d}{dt}(\text{IJV})$. All but one have high positive MCCCs and positive delays. GMS: global mean signal. MCCC: maximum cross-correlation coefficient. IJV: internal jugular vein.

4.3.3 Spatial-temporal information of the coupling of CSF inflow with the brain signal

Figure 4-5 shows the averaged MCCCs and delay maps derived from the voxel-wise cross-correlation between CSF inflow signal and $\frac{d}{dt}$ (fMRI signal). Negative MCCCs were found in most of the tissue-containing voxels with distributions shown in figure 4-5 (a). Regions with the highest negative MCCCs are found in the gray matter, especially in high blood density regions such as the visual cortex. It is worth noting that the positive correlations (shown in blue) were found in the voxels next to the lateral ventricles (Figure 4-5 (a,b)), likely due to partial volume effects.

Negative delays were found in most of the voxels with distributions shown in figure 4-5 (f). Negative delays indicate that $\frac{d}{dt}$ (fMRI signal) is leading CSF inflow signal. This result is consistent with the findings in figures 4-3 and 4-4. As we consider the changes in CBV as a cause for “pressure waves”, the delay map then represents the propagation of these waves in the brain. From figure 4-5 (d), we can see that they started from the precentral gyrus, and moved toward the regions surrounding the ventricles (red/yellow in figure 4-5 (d)). However, a few observations do not fit the proposed model. First, the voxels with the longest delays (red/yellow in figure 4-5 (d)), which cover much of the extended region from the ventricles into the white matter, do not overlap with the positively correlated voxels in figure 4-5 (a). Second, the delay values are positive, indicating they lag a few seconds after CSF inflow. Therefore, signals from these voxels still reflect CBV changes, but following CSF inflow, which might indicate there are secondary interactions between CSF inflow and white matter.

MCCC between $\frac{d}{dt}$ (fMRI signal) and CSF inflow signal

Delay time between $\frac{d}{dt}$ (fMRI signal) and CSF inflow signal

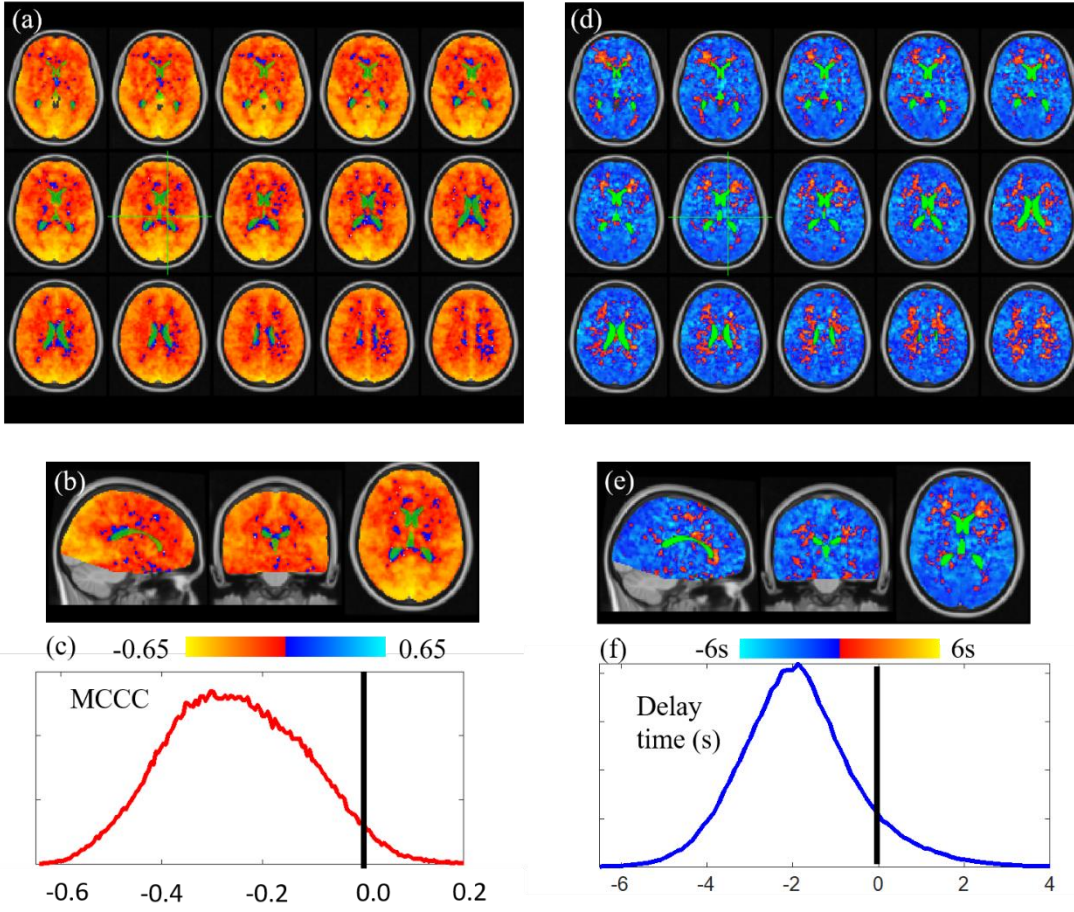


Figure 4-5 Group average of voxel-wise cross-correlation between $\frac{d}{dt}$ (fMRI signal) and CSF inflow signal. (a-b) Various views of whole-brain MCCCs show that most of the $\frac{d}{dt}$ (fMRI signal) in the brain were negatively (red-yellow) correlated with CSF inflow signal. (c) The distribution of MCCCs. (d-e) Various views of whole-brain delays show that most of the $\frac{d}{dt}$ (fMRI signal) is ahead of CSF inflow signal. (f) The distribution of the delays. MCCC: maximum cross-correlation coefficient.

4.4 Discussion

This study used a simple model to explain the correlation and delays between $\frac{d}{dt}$ (GMS) of fMRI and CSF flow measured at the fourth ventricle. With both brain and neck scans, we validated that CSF flow at low frequencies was bi-directional and found that coupling between the brain hemodynamics and CSF flow exists for awake participants in the supine position.

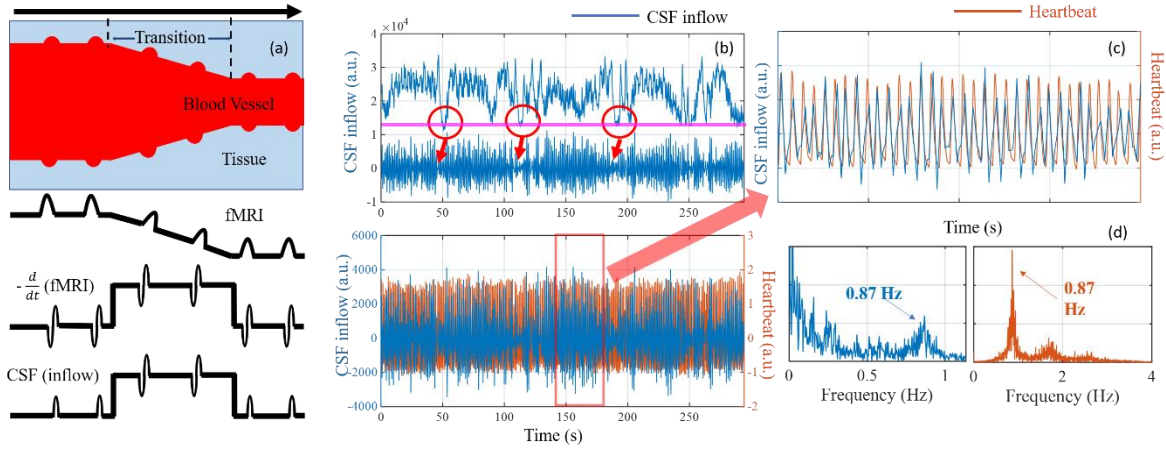


Figure 4-6 (a) The model depicts the low-frequency (e.g., vasomotion) and high-frequency (heartbeat) vessel volume changes and their impacts on the fMRI, and CSF inflow signals. (b) CSF inflow signal (upper panel: raw data of CSF inflow; lower panel: high pass filtered CSF inflow ($>0.6\text{Hz}$) to extract the heartbeat signal). Three red circles represent big drops of CSF inflow, which indicate CSF outflow or no flow. In these periods, smaller amplitudes of heartbeat signals are found (pointed by red arrows). (c) High-frequency CSF inflow signal ($>0.6\text{Hz}$, blue) and heartbeat signal recovered from the brain data using “Happy” (Aslan et al., 2019). (d) Power spectrum (arbitrary unit) of CSF inflow signal (left) and power spectrum of heartbeat signal (right). These two panels show that 1) the heartbeat signal can be detected in CSF inflow signal, which matched that of the brain; 2) little or no delay was found in the heartbeat signal in the brain and that detected in CSF inflow.

4.4.1 Possible driving forces for CSF flow

Previous studies have proposed several driving forces for CSF flow, which included 1) cardiac pulsation [133], 2) vasomotion [117], and 3) respiration [120, 134]. Some studies demonstrate that pulsation is a driving force for CSF [114, 133, 135]. However, others studies used a mathematical model to argue that arteriolar pulsation alone is too weak to drive CSF circulation [136, 137].

Figure 4-6 (b) is example data of CSF inflow taken from one participant’s head scan. It compares the effect of pulsation and slow arteriolar oscillation on CSF inflow. The LFOs are dominant in the signal, and thus are the main contributor to CSF flow. This is further confirmed by the power spectrum of the signal (Figure 4-6 (d)), in which the heartbeat signal ($\sim 0.87\text{Hz}$) is much smaller than that of LFOs. These LFO signals are associated with arteriolar slow oscillations, such as vasomotion created by rhythmic spontaneous contractions of vascular smooth muscle cells [117, 136, 138, 139]. On the same note, increased ultra-low frequency vasomotion (0.1 Hz) in arterioles was found to increase clearance rate from perivascular space [117].

To investigate the pulsatile CSF inflow and blood flow, we extracted the full cardiac pulsation waveform from the undersampled brain fMRI scan [140]. A section of the reconstructed

cardiac waveform is shown in figure 4-6 (c), together with the cardiac wave derived from CSF inflow signal by high-pass filtering (>0.6 Hz). These two signals match with no clear delays, likely because of the fast-traveling nature of cardiac pulsation.

Based on these findings, we adapted the model in figure 4-1 by adding the pulsatile oscillations. Thus, the model included both pulsatile and slow arteriolar oscillations on the blood vessels (Figure 4-6 (a)), in which, the faster and smaller pulsatile changes were added to the slow, bigger low-frequency changes. From the model, we can see that 1) inflow will be continuous during the slow transition period (as marked in figure 4-6 (a)). 2) The pulsations during this period will modulate the inflow speed (not reverse flow direction), thus the full scale of the derivative pulsatile signal is “recorded” by the fMRI. However, for the pulsations happening outside this period, they induced CSF flow in both directions. Therefore, only a partial signal (positive derivative pulsatile signal) was “recorded”. This explained why the magnitudes of heartbeat-related signals were bigger during the inflow period, and much smaller or invisible otherwise (circles in figure 4-6 (b)).

In addition to pulsation and vasomotion, several lines of work showed that respiration is instrumental in driving CSF through the aqueduct by real-time phase-contrast MRI measurements [118-120, 134, 141]. Furthermore, Dreha-Kulaczewski et al. proposed that increased CSF flow from caudal to cranial during inspiration was considered compensation of venous blood leaving from the head due to lower intrathoracic pressure [120]. Based on this theory (i.e., pressure), CSF inflow and blood outflow (i.e., vein) should happen simultaneously. however, we can only measure the LFO of CSF outflow and fMRI signal in IJV simultaneously in the neck scan. There are no consistent delays found between these two signals, yet the delay between CSF outflow and $\frac{d}{dt}$ (IJV) was about 0.66s (i.e., CSF leading $\frac{d}{dt}$ (IJV)). This result may support the “top model” that the original “engine” for CSF flow is from above, i.e., cerebrovascular oscillation (see figure 4-4), instead of the lung. As we discuss in 4.3.2, cerebrovascular slow oscillations move with blood through the brain slowly (take a few seconds). The oscillations will compress and expand lateral ventricles, which leads to CSF flow observed at the fourth ventricle. The same oscillations will eventually move to the vein and be observed at IJVs.

Our study focused on the LFO of the signal, not the respiration frequency. The natural breathing frequencies of our participants were from 0.2-0.4 Hz. Like cardiac pulsation, the power

of the respiration signal is much less than that of the LFOs, indicating that the arterial LFO is the dominant force in driving CSF flow, at least in resting-state without using any forced/paced breathing protocol. In addition, forced or paced breathing as used in Dreha-Kulaczewski's study might invoke different physiological responses/mechanisms, other than the ones under regular breathing [120].

This study and previous research found CSF flowed in both directions through the fourth ventricle [121]. To roughly assess the net flow, we calculated the areas under 1) the CSF inflow (from brain scan, figure 4-7 (a) (red)) and 2) CSF outflow (from neck scan, figure 4-7 (a) (blue)) for each subject. The difference represents the net amount of CSF flow during the time of scan for each participant (figure 4-7 (b)). It is known that the CSF inflow and outflow were measured consecutively in two separated scans. Thus, the calculation of the net flow is not strictly accurate and should be treated as an estimate. No consistent net flow direction was detected among participants, indicating the net flow was not substantial during the short scan time (i.e., # minutes). It is known that adult only secret 25 ml CSF/hour in the brain (mostly from the choroid plexuses of the lateral ventricles) [142]. The secretion creates a pressure that dictates the direction of CSF flow through the ventricular system to the subarachnoid space (net flow in one direction). However, due to the small amount, the net flow would be hard to detect during the short period of time with our imaging method.

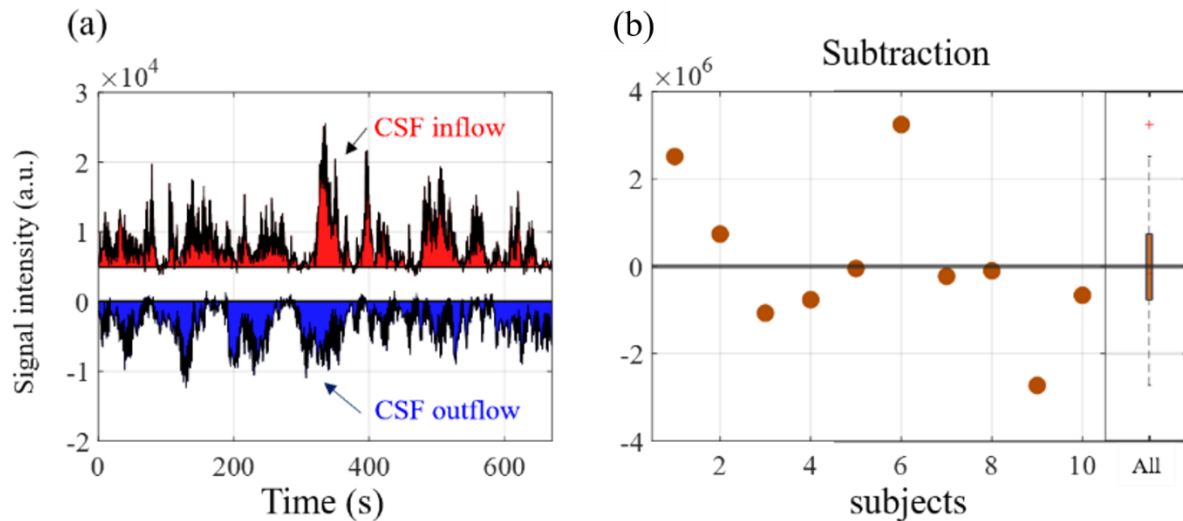


Figure 4-7 CSF net flow assessment. (a) Net flow measurements for CSF inflow (red) and outflow (blue) from one participant. (b) Net flow difference for all participants.

In summary, though our model explains the underlying mechanism between vessel volume dynamics and CSF flow, it does not discern the causes for the vessel dynamics. It is probable that multiple mechanisms contribute to facilitating CSF flow.

4.4.2 Ventricular vs. perivascular effects

Unlike fast traveling cardiac pulsation that reaches all the voxels in the brain at almost the same time, LFOs in BOLD fMRI (associated with vasomotion or arterial O_2 and CO_2 fluctuations) have been shown to propagate in the brain as the blood flow [18] and take up to 5s to transit the brain. The corresponding vessel dilation or pressure wave ($\frac{d}{dt}$ (fMRI signal)) is shown to have a clear spatial-temporal pattern in figure 4-5 (d), moving from an arterial-rich region to the white matter regions, then the vicinities of lateral ventricles in seconds. As a result, the ventricular wall might be compressed continuously and sequentially, not simultaneously as in the case of pulsation. This also explained the delay (1-2s) we observed in the LFO signals of CSF and $\frac{d}{dt}$ (fMRI signal), while, not in the cardiac pulsation signals (Figure 4-6).

It was evident that CSF tracers entered the parenchyma through a periarterial pathway and ex-vivo evidence showed that tracers rapidly exited the brain primarily along central deep veins and the lateral ventral caudal rhinal veins [113, 143]. This offers another pathway of CSF travel through perivascular structures. However, the fundamental driving force can still be arterial dilation and contraction. Instead of having an accumulative effect on the ventricles, the force will be exerted locally at the perivascular space. The exact pathways of CSF migration are not clear [138]. Nevertheless, the close underlying coupling between vessel volume changes and CSF flow could contribute to multiple pathways.

4.4.3 Sleep vs. awake states

Previous research documents increase in the cortical interstitial space by more than 60% during sleep when compared with an awake condition, resulting in efficient convective clearance of β -amyloid and other compounds [113]. This highly sleep-dependent clearance was observed in both human and mouse models [144, 145]. In our study, we demonstrated a strong coupling between brain hemodynamics and CSF movement in awake participants. It suggests that CSF (albeit not robust) is maintained during the waking hours. It would be of great interest to

understand the fundamental differences between sleep and the wakeful states, in terms of vasomotion, CSF flow, coupling, and overall efficiency of clearance of the inflammatory proteins and metabolites.

4.4.4 Limitation and future studies

There are several limitations to the study which we hope to address in future experiments. First, no respiration-related data was collected, including chest belt and $P_{ET}CO_2$ measurements. These data can help us understand the physiological mechanisms of the LFOs in the fMRI. Second, we did not collect simultaneous EEG data. Thus, we could not confirm if the same neuro-vascular coupling as was demonstrated in the sleeping study, works in the wakeful state. Third, the net flow was not accurately assessed in this study. In future studies, we will incorporate respiration and EEG measurements. Moreover, we will compare the regular and forced breathing, to understand the differences in the underlying mechanisms.

4.5 Conclusion

A biomechanical model was proposed in this study to explain the delayed coupling between $\frac{d}{dt}$ (GMS) and CSF flow. Two fMRI scans were conducted to validate our model and several predictions. We found 1) coupling existed between LFOs of $\frac{d}{dt}$ (fMRI signal) and CSF flow signals when participants were awake; 2) the LFOs of $\frac{d}{dt}$ (GMS) occurred about 2.2 seconds earlier than those of CSF inflow; 3) CSF flow at the fourth ventricle is bi-directional by fMRI. Together, we conclude that the arterial LFO is the dominant force in driving CSF flow during wakefulness. These findings can help understand the mechanics of CSF flow and develop new interventions to increase the clearance rate in the brain, especially for patients with neurodegenerative diseases.

5. CONCLUSION

My work can be summarized in two folds. First, I studied physiological effects on brain using multimodel imagings. By using innovative methods on conventional imaging modality, vascular effects on the brain can be explored and used to be compared with neuronal finidng. Also, by having concurrent experiment using multiple imaging modalities, I was able to adjust original experimental design and translate the conventional measurement to a more portable, convenient measurement. Second, I established a model to interpret the interaction between cerebral physiological signal and its interaction with cerebrospinal fluid, another system which is highly related to the clearance of cerebral waste product. All my work have the potential to investigate drug effect on the brain and neurodegenerative diseases.

REFERENCES

1. Walter, W.G., *The convergence and interaction of visual, auditory, and tactile responses in human nonspecific cortex*. Annals of the New York Academy of Sciences, 1964. **112**(1): p. 320-361.
2. Rao, A., H. Hu, and A.C. Nobre, *The effects of combined caffeine and glucose drinks on attention in the human brain*. Nutritional neuroscience, 2005. **8**(3): p. 141-153.
3. Garavan, H., et al., *Cue-induced cocaine craving: neuroanatomical specificity for drug users and drug stimuli*. American journal of psychiatry, 2000. **157**(11): p. 1789-1798.
4. Poulin, M., P. Liang, and P. Robbins, *Dynamics of the cerebral blood flow response to step changes in end-tidal PCO₂ and PO₂ in humans*. Journal of Applied Physiology, 1996. **81**(3): p. 1084-1095.
5. Stephan, H., et al., *Effect of Disoprivan (propofol) on the circulation and oxygen consumption of the brain and CO₂ reactivity of brain vessels in the human*. Der Anaesthesist, 1987. **36**(2): p. 60-65.
6. Kaisti, K.K., et al., *Effects of sevoflurane, propofol, and adjunct nitrous oxide on regional cerebral blood flow, oxygen consumption, and blood volume in humans*. Anesthesiology: The Journal of the American Society of Anesthesiologists, 2003. **99**(3): p. 603-613.
7. Qiu, M., et al., *Multi-modal analysis of functional connectivity and cerebral blood flow reveals shared and unique effects of propofol in large-scale brain networks*. Neuroimage, 2017. **148**: p. 130-140.
8. Birn, R.M., et al., *The respiration response function: the temporal dynamics of fMRI signal fluctuations related to changes in respiration*. Neuroimage, 2008. **40**(2): p. 644-654.
9. Birn, R.M., et al., *Separating respiratory-variation-related fluctuations from neuronal-activity-related fluctuations in fMRI*. Neuroimage, 2006. **31**(4): p. 1536-1548.
10. Chang, C., J.P. Cunningham, and G.H. Glover, *Influence of heart rate on the BOLD signal: the cardiac response function*. Neuroimage, 2009. **44**(3): p. 857-869.
11. Wise, R.G., et al., *Resting fluctuations in arterial carbon dioxide induce significant low frequency variations in BOLD signal*. Neuroimage, 2004. **21**(4): p. 1652-1664.
12. Shmueli, K., et al., *Low-frequency fluctuations in the cardiac rate as a source of variance in the resting-state fMRI BOLD signal*. Neuroimage, 2007. **38**(2): p. 306-320.
13. Zarahn, E., G.K. Aguirre, and M. D'Esposito, *Empirical analyses of BOLD fMRI statistics*. Neuroimage, 1997. **5**(3): p. 179-197.
14. Power, J.D., et al., *Methods to detect, characterize, and remove motion artifact in resting state fMRI*. Neuroimage, 2014. **84**: p. 320-341.
15. Tong, Y., *Time lag dependent multimodal processing of concurrent fMRI and near-infrared spectroscopy (NIRS) data suggests a global circulatory origin for low-frequency oscillation signals in human brain*. Neuroimage, 2010. **53**(2): p. 553-564.
16. Tong, Y., *Concurrent fNIRS and fMRI processing allows independent visualization of the propagation of pressure waves and bulk blood flow in the cerebral vasculature*. Neuroimage, 2012. **61**(4): p. 1419-1427.
17. Tong, Y., *Tracking cerebral blood flow in BOLD fMRI using recursively generated regressors*. Human brain mapping, 2014. **35**(11): p. 5471-5485.

18. Tong, Y., et al., *Perfusion information extracted from resting state functional magnetic resonance imaging*. Journal of Cerebral Blood Flow & Metabolism, 2017. **37**(2): p. 564-576.
19. Liu, P., et al., *Multiparametric imaging of brain hemodynamics and function using gas-inhalation MRI*. NeuroImage, 2017. **146**: p. 715-723.
20. Yang, H.C., et al., *Vascular effects of caffeine found in BOLD fMRI*. Journal of neuroscience research, 2019. **97**(4): p. 456-466.
21. Bandettini, P.A., et al., *Time course EPI of human brain function during task activation*. Magnetic resonance in medicine, 1992. **25**(2): p. 390-397.
22. Ogawa, S., et al., *Intrinsic signal changes accompanying sensory stimulation: functional brain mapping with magnetic resonance imaging*. Proceedings of the National Academy of Sciences, 1992. **89**(13): p. 5951-5955.
23. Hoge, R.D., et al., *Investigation of BOLD signal dependence on cerebral blood flow and oxygen consumption: the deoxyhemoglobin dilution model*. Magnetic resonance in medicine, 1999. **42**(5): p. 849-863.
24. D'Esposito, M., L.Y. Deouell, and A. Gazzaley, *Alterations in the BOLD fMRI signal with ageing and disease: a challenge for neuroimaging*. Nature Reviews Neuroscience, 2003. **4**(11): p. 863.
25. Buxton, R.B., et al., *Modeling the hemodynamic response to brain activation*. Neuroimage, 2004. **23**: p. S220-S233.
26. Vigneau-Roy, N., et al., *Regional variations in vascular density correlate with resting-state and task-evoked blood oxygen level-dependent signal amplitude*. Human brain mapping, 2014. **35**(5): p. 1906-1920.
27. Hocke, L.M., et al., *Comparison of peripheral near-infrared spectroscopy low-frequency oscillations to other denoising methods in resting state functional MRI with ultrahigh temporal resolution*. Magnetic resonance in medicine, 2016. **76**(6): p. 1697-1707.
28. Julien, C., *The enigma of Mayer waves: facts and models*. Cardiovascular research, 2006. **70**(1): p. 12-21.
29. Golestani, A.M., et al., *The association between cerebrovascular reactivity and resting-state fMRI functional connectivity in healthy adults: The influence of basal carbon dioxide*. Neuroimage, 2016. **132**: p. 301-313.
30. Tong, Y., et al., *Evaluating the effects of systemic low frequency oscillations measured in the periphery on the independent component analysis results of resting state networks*. Neuroimage, 2013. **76**: p. 202-215.
31. Tong, Y., et al., *The resting-state fMRI arterial signal predicts differential blood transit time through the brain*. Journal of Cerebral Blood Flow & Metabolism, 2018: p. 0271678X17753329.
32. Strangman, G., et al., *A quantitative comparison of simultaneous BOLD fMRI and NIRS recordings during functional brain activation*. Neuroimage, 2002. **17**(2): p. 719-731.
33. Kannurpatti, S.S., et al., *Spatio-temporal characteristics of low-frequency BOLD signal fluctuations in isoflurane-anesthetized rat brain*. Neuroimage, 2008. **40**(4): p. 1738-1747.
34. Rack-Gomer, A.L., J. Liau, and T.T. Liu, *Caffeine reduces resting-state BOLD functional connectivity in the motor cortex*. Neuroimage, 2009. **46**(1): p. 56-63.
35. Hindmarch, I., et al., *A naturalistic investigation of the effects of day-long consumption of tea, coffee and water on alertness, sleep onset and sleep quality*. Psychopharmacology, 2000. **149**(3): p. 203-216.

36. Liu, T.T., et al., *Caffeine alters the temporal dynamics of the visual BOLD response*. Neuroimage, 2004. **23**(4): p. 1402-1413.
37. Liao, J., J.E. Perthen, and T.T. Liu, *Caffeine reduces the activation extent and contrast-to-noise ratio of the functional cerebral blood flow response but not the BOLD response*. Neuroimage, 2008. **42**(1): p. 296-305.
38. Behzadi, Y. and T.T. Liu, *Caffeine reduces the initial dip in the visual BOLD response at 3 T*. Neuroimage, 2006. **32**(1): p. 9-15.
39. Tal, O., et al., *Caffeine-induced global reductions in resting-state BOLD connectivity reflect widespread decreases in MEG connectivity*. Frontiers in human neuroscience, 2013. **7**.
40. Wu, W.C., et al., *Caffeine alters resting-state functional connectivity measured by blood oxygenation level-dependent MRI*. NMR in biomedicine, 2014. **27**(4): p. 444-452.
41. Mathew, R.J. and W.H. Wilson, *Caffeine induced changes in cerebral circulation*. Stroke, 1985. **16**(5): p. 814-817.
42. Addicott, M.A., et al., *The effect of daily caffeine use on cerebral blood flow: how much caffeine can we tolerate?* Human brain mapping, 2009. **30**(10): p. 3102-3114.
43. Griffeth, V.E., J.E. Perthen, and R.B. Buxton, *Prospects for quantitative fMRI: investigating the effects of caffeine on baseline oxygen metabolism and the response to a visual stimulus in humans*. Neuroimage, 2011. **57**(3): p. 809-816.
44. Poldrack, R.A., et al., *Long-term neural and physiological phenotyping of a single human*. Nature communications, 2015. **6**: p. 8885.
45. Jenkinson, M., et al., *Fsl*. Neuroimage, 2012. **62**(2): p. 782-790.
46. Tong, Y. and B.d. Frederick, *Tracking cerebral blood flow in BOLD fMRI using recursively generated regressors*. Human brain mapping, 2014. **35**(11): p. 5471-5485.
47. Daniel, W.W., *Kolmogorov-Smirnov one-sample test*. Applied Nonparametric Statistics, 1990: p. 319-330.
48. Gordon, E.M., et al., *Generation and evaluation of a cortical area parcellation from resting-state correlations*. Cerebral cortex, 2014. **26**(1): p. 288-303.
49. Laumann, T.O., et al., *Functional system and areal organization of a highly sampled individual human brain*. Neuron, 2015. **87**(3): p. 657-670.
50. Cameron, O.G., J.G. Modell, and M. Hariharan, *Caffeine and human cerebral blood flow: a positron emission tomography study*. Life sciences, 1990. **47**(13): p. 1141-1146.
51. Wong, C.W., et al., *Anti-correlated networks, global signal regression, and the effects of caffeine in resting-state functional MRI*. Neuroimage, 2012. **63**(1): p. 356-364.
52. James, J.E., *Critical review of dietary caffeine and blood pressure: a relationship that should be taken more seriously*. Psychosomatic medicine, 2004. **66**(1): p. 63-71.
53. Lunt, M., et al., *Comparison of caffeine-induced changes in cerebral blood flow and middle cerebral artery blood velocity shows that caffeine reduces middle cerebral artery diameter*. Physiological measurement, 2004. **25**(2): p. 467.
54. Kim, S.G., et al., *Potential pitfalls of functional MRI using conventional gradient-recalled echo techniques*. NMR in Biomedicine, 1994. **7**(1-2): p. 69-74.
55. Mulderink, T.A., et al., *On the use of caffeine as a contrast booster for BOLD fMRI studies*. Neuroimage, 2002. **15**(1): p. 37-44.
56. Buch, S., Y. Ye, and E.M. Haacke, *Quantifying the changes in oxygen extraction fraction and cerebral activity caused by caffeine and acetazolamide*. Journal of Cerebral Blood Flow & Metabolism, 2017. **37**(3): p. 825-836.

57. Merola, A., et al., *Mapping the pharmacological modulation of brain oxygen metabolism: The effects of caffeine on absolute CMRO2 measured using dual calibrated fMRI*. NeuroImage, 2017. **155**: p. 331-343.
58. Rowe, G.G., et al., *A study in man of cerebral blood flow and cerebral glucose, lactate and pyruvate metabolism before and after eating*. The Journal of clinical investigation, 1959. **38**(12): p. 2154-2158.
59. McCusker, R.R., B.A. Goldberger, and E.J. Cone, *Caffeine content of specialty coffees*. Journal of analytical toxicology, 2003. **27**(7): p. 520-522.
60. Sedlacik, J., et al., *Investigations on the effect of caffeine on cerebral venous vessel contrast by using susceptibility-weighted imaging (SWI) at 1.5, 3 and 7 T*. Neuroimage, 2008. **40**(1): p. 11-18.
61. Yang, H.C., et al., *Characterizing near-infrared spectroscopy signal under hypercapnia*. Journal of Biophotonics, 2020. **13**(11): p. e202000173.
62. Faraci, F.M., K.R. Breese, and D.D. Heistad, *Cerebral vasodilation during hypercapnia. Role of glibenclamide-sensitive potassium channels and nitric oxide*. Stroke, 1994. **25**(8): p. 1679-1683.
63. Davis, T.L., et al., *Calibrated functional MRI: mapping the dynamics of oxidative metabolism*. Proceedings of the National Academy of Sciences, 1998. **95**(4): p. 1834-1839.
64. Chiarelli, P.A., et al., *Flow-metabolism coupling in human visual, motor, and supplementary motor areas assessed by magnetic resonance imaging*. Magnetic Resonance in Medicine: An Official Journal of the International Society for Magnetic Resonance in Medicine, 2007. **57**(3): p. 538-547.
65. Yoon, S.H., M. Zuccarello, and R.M. Rapoport, *Reversal of hypercapnia induces endothelin-dependent constriction of basilar artery in rabbits with acute metabolic alkalosis*. General Pharmacology: The Vascular System, 2000. **35**(6): p. 333-340.
66. Lassen, N., *Brain extracellular pH: the main factor controlling cerebral blood flow*. 1968, Taylor & Francis.
67. Stefanovic, B., et al., *Hemodynamic and metabolic responses to activation, deactivation and epileptic discharges*. Neuroimage, 2005. **28**(1): p. 205-215.
68. Barten, C.W. and E.S. Wang, *Correlation of end-tidal CO2 measurements to arterial PaCO2 in nonintubated patients*. Annals of emergency medicine, 1994. **23**(3): p. 560-563.
69. Prisman, E., et al., *Comparison of the effects of independently-controlled end-tidal PCO2 and PO2 on blood oxygen level-dependent (BOLD) MRI*. Journal of Magnetic Resonance Imaging: An Official Journal of the International Society for Magnetic Resonance in Medicine, 2008. **27**(1): p. 185-191.
70. Rostrup, E., et al., *Functional MRI of CO2 induced increase in cerebral perfusion*. NMR in Biomedicine, 1994. **7**(1-2): p. 29-34.
71. Yezhuvath, U.S., et al., *On the assessment of cerebrovascular reactivity using hypercapnia BOLD MRI*. NMR in Biomedicine: An International Journal Devoted to the Development and Application of Magnetic Resonance In vivo, 2009. **22**(7): p. 779-786.
72. Wise, R.G., et al., *Dynamic forcing of end-tidal carbon dioxide and oxygen applied to functional magnetic resonance imaging*. Journal of Cerebral Blood Flow & Metabolism, 2007. **27**(8): p. 1521-1532.
73. Slessarev, M., et al., *Prospective targeting and control of end-tidal CO2 and O2 concentrations*. The Journal of physiology, 2007. **581**(3): p. 1207-1219.

74. Kastrup, A., et al., *Functional magnetic resonance imaging of regional cerebral blood oxygenation changes during breath holding*. Stroke, 1998. **29**(12): p. 2641-2645.
75. Markus, H. and M. Harrison, *Estimation of cerebrovascular reactivity using transcranial Doppler, including the use of breath-holding as the vasodilatory stimulus*. Stroke, 1992. **23**(5): p. 668-673.
76. Boas, D.A., et al., *Twenty years of functional near-infrared spectroscopy: introduction for the special issue*. 2014, Elsevier.
77. Ferrari, M. and V. Quaresima, *A brief review on the history of human functional near-infrared spectroscopy (fNIRS) development and fields of application*. Neuroimage, 2012. **63**(2): p. 921-935.
78. Scholkmann, F., et al., *A review on continuous wave functional near-infrared spectroscopy and imaging instrumentation and methodology*. Neuroimage, 2014. **85**: p. 6-27.
79. Wolf, M., M. Ferrari, and V. Quaresima, *Progress of near-infrared spectroscopy and topography for brain and muscle clinical applications*. Journal of biomedical optics, 2007. **12**(6): p. 062104.
80. Svaldi, D.O., et al., *Cerebrovascular reactivity alterations in asymptomatic high school football players*. Developmental neuropsychology, 2015. **40**(2): p. 80-84.
81. Svaldi, D.O., et al., *Cerebrovascular reactivity changes in asymptomatic female athletes attributable to high school soccer participation*. Brain imaging and behavior, 2017. **11**(1): p. 98-112.
82. Svaldi, D.O., et al., *Accumulation of high magnitude acceleration events predicts cerebrovascular reactivity changes in female high school soccer athletes*. Brain imaging and behavior, 2018: p. 1-11.
83. Riecker, A., et al., *Relation between regional functional MRI activation and vascular reactivity to carbon dioxide during normal aging*. Journal of Cerebral Blood Flow & Metabolism, 2003. **23**(5): p. 565-573.
84. Schieve, J.F. and W.P. Wilson, *The influence of age, anesthesia and cerebral arteriosclerosis on cerebral vascular activity to CO₂*. The American journal of medicine, 1953. **15**(2): p. 171-174.
85. Smielewski, P., et al., *Can cerebrovascular reactivity be measured with near-infrared spectroscopy?* Stroke, 1995. **26**(12): p. 2285-2292.
86. Emir, U., C. Ozturk, and A. Akin, *Multimodal investigation of fMRI and fNIRS derived breath hold BOLD signals with an expanded balloon model*. Physiological measurement, 2007. **29**(1): p. 49.
87. Leung, T.S., et al., *Estimating a modified Grubb's exponent in healthy human brains with near infrared spectroscopy and transcranial Doppler*. Physiological measurement, 2008. **30**(1): p. 1.
88. Virtanen, J., T.E. Noponen, and P. Meriläinen, *Comparison of principal and independent component analysis in removing extracerebral interference from near-infrared spectroscopy signals*. Journal of biomedical optics, 2009. **14**(5): p. 054032.
89. Selb, J.J., et al., *Sensitivity of near-infrared spectroscopy and diffuse correlation spectroscopy to brain hemodynamics: simulations and experimental findings during hypercapnia*. Neurophotonics, 2014. **1**(1): p. 015005.
90. Alderliesten, T., et al., *Simultaneous quantitative assessment of cerebral physiology using respiratory-calibrated MRI and near-infrared spectroscopy in healthy adults*. Neuroimage, 2014. **85**: p. 255-263.

91. MacIntosh, B.J., L.M. Klassen, and R.S. Menon, *Transient hemodynamics during a breath hold challenge in a two part functional imaging study with simultaneous near-infrared spectroscopy in adult humans*. NeuroImage, 2003. **20**(2): p. 1246-1252.
92. Gagnon, L., et al., *Quantification of the cortical contribution to the NIRS signal over the motor cortex using concurrent NIRS-fMRI measurements*. Neuroimage, 2012. **59**(4): p. 3933-3940.
93. Funane, T., et al., *Quantitative evaluation of deep and shallow tissue layers' contribution to fNIRS signal using multi-distance optodes and independent component analysis*. Neuroimage, 2014. **85**: p. 150-165.
94. Harris, D., F. Cowans, and D. Wertheim, *NIRS in the temporal region-strong influence of external carotid artery*, in *Oxygen Transport to Tissue XV*. 1994, Springer. p. 825-828.
95. Duffin, J., et al., *The role of vascular resistance in BOLD responses to progressive hypercapnia*. Human brain mapping, 2017. **38**(11): p. 5590-5602.
96. Bright, M.G. and K. Murphy, *Reliable quantification of BOLD fMRI cerebrovascular reactivity despite poor breath-hold performance*. NeuroImage, 2013. **83**: p. 559-568.
97. Peirce, J., et al., *PsychoPy2: Experiments in behavior made easy*. Behavior research methods, 2019: p. 1-9.
98. Tancredi, F.B. and R.D. Hoge, *Comparison of cerebral vascular reactivity measures obtained using breath-holding and CO₂ inhalation*. Journal of Cerebral Blood Flow & Metabolism, 2013. **33**(7): p. 1066-1074.
99. Xu, Y., H.L. Graber, and R.L. Barbour. *nirsLAB: a computing environment for fNIRS neuroimaging data analysis*. in *Biomedical Optics*. 2014. Optical Society of America.
100. Shen, X., et al., *Groupwise whole-brain parcellation from resting-state fMRI data for network node identification*. Neuroimage, 2013. **82**: p. 403-415.
101. Fisher, R.A., *Frequency distribution of the values of the correlation coefficient in samples from an indefinitely large population*. Biometrika, 1915. **10**(4): p. 507-521.
102. Fisher, R.A., *On the 'probable error' of a coefficient of correlation deduced from a small sample*. Metron, 1921. **1**: p. 1-32.
103. Genovese, C.R., N.A. Lazar, and T. Nichols, *Thresholding of statistical maps in functional neuroimaging using the false discovery rate*. Neuroimage, 2002. **15**(4): p. 870-878.
104. McCormick, P.W., et al., *Intracerebral penetration of infrared light*. Journal of neurosurgery, 1992. **76**(2): p. 315-318.
105. Saager, R.B. and A.J. Berger, *Direct characterization and removal of interfering absorption trends in two-layer turbid media*. JOSA A, 2005. **22**(9): p. 1874-1882.
106. Paulson, O., S. Strandgaard, and L. Edvinsson, *Cerebral autoregulation*. Cerebrovascular and brain metabolism reviews, 1990. **2**(2): p. 161-192.
107. Van Bel, F., et al., *The influence of indomethacin on the autoregulatory ability of the cerebral vascular bed in the newborn lamb*. Pediatric research, 1993. **34**(2): p. 178.
108. Sato, K., et al., *Differential blood flow responses to CO₂ in human internal and external carotid and vertebral arteries*. The Journal of physiology, 2012. **590**(14): p. 3277-3290.
109. Vantanajal, J.S., et al., *Differential sensitivities of cerebral and brachial blood flow to hypercapnia in humans*. Journal of Applied Physiology, 2007. **102**(1): p. 87-93.
110. Murphy, K., A.D. Harris, and R.G. Wise, *Robustly measuring vascular reactivity differences with breath-hold: normalising stimulus-evoked and resting state BOLD fMRI data*. Neuroimage, 2011. **54**(1): p. 369-379.

111. Huppert, T.J., et al., *A temporal comparison of BOLD, ASL, and NIRS hemodynamic responses to motor stimuli in adult humans*. Neuroimage, 2006. **29**(2): p. 368-382.
112. Boas, D.A., et al., *The accuracy of near infrared spectroscopy and imaging during focal changes in cerebral hemodynamics*. Neuroimage, 2001. **13**(1): p. 76-90.
113. Xie, L., et al., *Sleep drives metabolite clearance from the adult brain*. science, 2013. **342**(6156): p. 373-377.
114. Iliff, J.J., et al., *Cerebral arterial pulsation drives paravascular CSF–interstitial fluid exchange in the murine brain*. Journal of Neuroscience, 2013. **33**(46): p. 18190-18199.
115. Aalling, N., et al., *The Glymphatic System*. SHORT COURSE, 2017: p. 27.
116. Mestre, H., et al., *Flow of cerebrospinal fluid is driven by arterial pulsations and is reduced in hypertension*. Nature communications, 2018. **9**(1): p. 1-9.
117. van Veluw, S.J., et al., *Vasomotion as a driving force for paravascular clearance in the awake mouse brain*. Neuron, 2020. **105**(3): p. 549-561. e5.
118. Chen, L., et al., *Dynamics of respiratory and cardiac CSF motion revealed with real-time simultaneous multi-slice EPI velocity phase contrast imaging*. Neuroimage, 2015. **122**: p. 281-287.
119. Dreha-Kulaczewski, S., et al., *Inspiration is the major regulator of human CSF flow*. Journal of neuroscience, 2015. **35**(6): p. 2485-2491.
120. Dreha-Kulaczewski, S., et al., *Identification of the upward movement of human CSF in vivo and its relation to the brain venous system*. Journal of Neuroscience, 2017. **37**(9): p. 2395-2402.
121. Matsumae, M., et al., *Changing the currently held concept of cerebrospinal fluid dynamics based on shared findings of cerebrospinal fluid motion in the cranial cavity using various types of magnetic resonance imaging techniques*. Neurologia medico-chirurgica, 2019. **59**(4): p. 133.
122. Feinberg, D.A. and A.S. Mark, *Human brain motion and cerebrospinal fluid circulation demonstrated with MR velocity imaging*. Radiology, 1987. **163**(3): p. 793-799.
123. Yamada, S., et al., *Visualization of cerebrospinal fluid movement with spin labeling at MR imaging: preliminary results in normal and pathophysiologic conditions*. Radiology, 2008. **249**(2): p. 644-652.
124. Jaeger, E., et al., *Compressed-sensing accelerated 4D flow MRI of cerebrospinal fluid dynamics*. Fluids and Barriers of the CNS, 2020. **17**(1): p. 1-11.
125. Fultz, N.E., et al., *Coupled electrophysiological, hemodynamic, and cerebrospinal fluid oscillations in human sleep*. Science, 2019. **366**(6465): p. 628-631.
126. Duyn, J.H., et al., *Inflow versus deoxyhemoglobin effects in BOLD functional MRI using gradient echoes at 1.5 T*. NMR in Biomedicine, 1994. **7**(1-2): p. 83-88.
127. Mokri, B., *The Monroe–Kellie hypothesis: applications in CSF volume depletion*. Neurology, 2001. **56**(12): p. 1746-1748.
128. Delaidelli, A. and A. Moiraghi, *Respiration: a new mechanism for CSF circulation?* Journal of Neuroscience, 2017. **37**(30): p. 7076-7078.
129. Dreha-Kulaczewski, S., et al., *Respiration and the watershed of spinal CSF flow in humans*. Scientific reports, 2018. **8**(1): p. 1-7.
130. Spijkerman, J.M., et al., *Phase contrast MRI measurements of net cerebrospinal fluid flow through the cerebral aqueduct are confounded by respiration*. Journal of Magnetic Resonance Imaging, 2019. **49**(2): p. 433-444.

131. Zhang, Y., M. Brady, and S. Smith, *Segmentation of brain MR images through a hidden Markov random field model and the expectation-maximization algorithm*. IEEE transactions on medical imaging, 2001. **20**(1): p. 45-57.
132. Tong, Y., et al., *The resting-state fMRI arterial signal predicts differential blood transit time through the brain*. Journal of Cerebral Blood Flow & Metabolism, 2019. **39**(6): p. 1148-1160.
133. Schley, D., et al., *Mechanisms to explain the reverse perivascular transport of solutes out of the brain*. Journal of theoretical biology, 2006. **238**(4): p. 962-974.
134. Klose, U., et al., *Detection of a relation between respiration and CSF pulsation with an echoplanar technique*. Journal of Magnetic Resonance Imaging, 2000. **11**(4): p. 438-444.
135. Wang, P. and W.L. Olbricht, *Fluid mechanics in the perivascular space*. Journal of theoretical biology, 2011. **274**(1): p. 52-57.
136. Diem, A.K., et al., *Arterial pulsations cannot drive intramural periarterial drainage: significance for A β drainage*. Frontiers in neuroscience, 2017. **11**: p. 475.
137. Asgari, M., D. De Zélicourt, and V. Kurtcuoglu, *Glymphatic solute transport does not require bulk flow*. Scientific reports, 2016. **6**: p. 38635.
138. Albargothy, N.J., et al., *Convective influx/glymphatic system: tracers injected into the CSF enter and leave the brain along separate periarterial basement membrane pathways*. Acta neuropathologica, 2018. **136**(1): p. 139-152.
139. Aldea, R., et al., *Cerebrovascular smooth muscle cells as the drivers of intramural periarterial drainage of the brain*. Frontiers in aging neuroscience, 2019. **11**: p. 1.
140. Aslan, S., et al., *Extraction of the cardiac waveform from simultaneous multislice fMRI data using slice sorted averaging and a deep learning reconstruction filter*. Neuroimage, 2019. **198**: p. 303-316.
141. Yamada, S., et al., *Influence of respiration on cerebrospinal fluid movement using magnetic resonance spin labeling*. Fluids and barriers of the CNS, 2013. **10**(1): p. 36.
142. Telano, L.N. and S. Baker, *Physiology, Cerebral Spinal Fluid (CSF)*. StatPearls [Internet], 2020.
143. Nedergaard, M., *Garbage truck of the brain*. Science, 2013. **340**(6140): p. 1529-1530.
144. Kang, J.-E., et al., *Amyloid- β dynamics are regulated by orexin and the sleep-wake cycle*. Science, 2009. **326**(5955): p. 1005-1007.
145. Bateman, R.J., et al., *Human amyloid- β synthesis and clearance rates as measured in cerebrospinal fluid in vivo*. Nature medicine, 2006. **12**(7): p. 856-861.